## ABSTRACT

UPADHYE, SAMEER AMARNATH. Development of a Novel Active Ankle Prosthetic with Variable Passive Compliance and Equilibrium Angle (Under the direction of Dr. Gregory Buckner and Dr. He 'Helen' Huang).

Lower-limb amputations severely impact over 600,000 people living in the United States, causing significant hurdles for a healthy living. With projections showing an increasing trend in affected populations, the development of effective prosthetic devices is imperative. Currently, most commercially available prosthetic devices are passive, i.e. utilizing spring mechanisms for rehabilitation. These devices, however, fail to provide the essential energy injection for efficient ambulation. Hence, a large body of recent research has focused on the development of powered devices with high torque and power density. By coupling active with parallel passive elements, several research groups have developed promising powered prosthetics. However, most of the actuators used in these designs suffer from issues with maintenance, assembly requirements, and backdrivability. Furthermore, in a bid to fine-tune these devices for walking, most powered devices have passive elements with fixed characteristics. This imposes severe limitations on the range of motion and thereby the device's utility across different gait schemes. Hence, this study proposes a novel directly-driven embedded ball screw actuator with a modular spring design that addresses the aforementioned issues. Experimental tests validate the device's motion and torque bandwidth, backdrivability, spring characteristics, and impedance control characteristics.

# Development of a Novel Active Ankle Prosthetic with Variable Passive Compliance and Equilibrium Angle

by
Sameer Amarnath Upadhye

A thesis submitted to the Graduate Faculty of
North Carolina State University
in partial fulfillment of the
requirements for the degree of
Master of Science

Mechanical Engineering

Raleigh, North Carolina
2020

APPROVED BY:

| | |
|---|---|
| _____ | _____ |
| Dr. Gregory Buckner | Dr. He 'Helen' Huang |
| Committee Co-Chair | Committee Co-Chair |

_____
Dr. Scott Ferguson

## BIOGRAPHY

Sameer Upadhye pursued a master's degree with the Mechanical and Aerospace Engineering Department at North Carolina State University. He received his bachelor's degree in Mechanical Engineering from VJTI (University of Mumbai). He then worked for two years at L&T Heavy Engineering, working on the planning and manufacturing of hydraulic and hydro-pneumatic systems before deciding to pursue his master's degree at NCSU. At NCSU, he spent a year and half of his master's program working at the Neuromuscular Rehabilitation Engineering Lab. His research under the guidance of Dr. He 'Helen' Huang and Dr. Gregory Buckner, focused on the development of a novel powered ankle prosthesis with direct application in amputee rehabilitation.

## ACKNOWLEDGMENTS

The author would like to thank several researchers and staff in the UNC/NC State Joint Department of Biomedical Engineering and the Mechanical and Aerospace Engineering Department at North Carolina State University for their key contributions to the work described here. Dr. Gregory Buckner (Director, Electro-Mechanics Research Laboratory) co-advised the author, and Dr. He 'Helen' Huang (Director, Neuromuscular Rehabilitation Engineering Laboratory) co-advised and supported the work. John Cameron (Research Fabrication Facility Supervisor) and Vincent Chicarelli (Specialty Trades Technician) provided expert design, manufacturing guidance, and quality workmanship on the manufacturing and assembly of the ankle prosthesis. Dr. Ming Liu and Albert Dodson provided much-required mentorship on the mechanical design detailing. Dr. Xikai Tu and Dr. Ming Liu helped the author throughout on the electronics. The author would like to offer special thanks to Chinmay Shah for help during the final testing of the device and Dr. Varun Nalam for help in refining this document. The author would like to thank all other members of the Neuromuscular Rehabilitation Engineering Laboratory (NREL): Dr. I-Chieh Lee, Dr. Rajat Emanuel Singh, Bretta Fylstra, Aaron Fleming, Minhan Li, Robert Hinson, Ashling Lupiani, Noah Rubin, Wentao Liu, Joseph Berman, Fiona Popp, Brendan Driscoll, Aubrey Gray, Abbas Allili, Dr. Boxuan Zhong, Dr. Lizhi Pan, and Dr. Yue Wen while also thanking Dr. Stefan Atay and Dr. Shaphan Jerningan and Samuel Miller from the Electro-Mechanics Research Laboratory for their support, collaborative work, and helpful discussions.

The author would like to acknowledge the funding sources for this study. This research was partially supported by the National Science Foundation through award 1808898 and the National Health Institute through award 5R01EB024570-02.

# TABLE OF CONTENTS

# LIST OF TABLES

## LIST OF FIGURES

# CHAPTER 1. INTRODUCTION

## 1.1 Motivation

Lower-limb amputations negatively impact the quality of life of over 600,000 people living in the United States; the associated loss of mobility creates hurdles for healthy independent living (Hagberg, and Brånemark, 2001; Legro, *et al.*, 1999; Zidarov, *et al.*, 2009; Ziegler-Graham, *et al.*, 2008). It is projected that the number of lower-limb amputees will increase more than 100% by the year 2050, fueled by increases in median age and rates of dysvascular disease (Ziegler-Graham, *et al.*, 2008). The most common type of lower-limb amputation and the focus of this research work, unilateral transtibial amputation, negatively affects walking performance via increased metabolic cost, decreased walking speed, and reduced balance (Hsu, *et al.*, 2006; Lehmann, *et al.*, 1993; Miller, *et al.*, 2001; Torburn, *et al.*, 1990; Waters, and Mulroy, 1999). The development of high torque, low weight, and efficient ankle prosthetic devices is essential for improving the quality of life for lower-limb prosthetic patients.

## 1.2 Lower limb prosthesis research and proposal

Most commercially available below-knee prosthetic devices are entirely passive devices; they feature linear or non-linear spring-like elements designed to mimic human biomechanics[1] by passively storing and releasing energy during specific phases of the gait cycle (Au, Samuel, *et al.*, 2008; Voloshina, and Collins, 2019). However, their passive mechanical characteristics prohibit the injection of active power into the gait cycle, in stark contrast to biological lower-limb muscles which provide up to 80% of the mechanical work per step (Voloshina, and Collins, 2019). Whereas the human ankle can vary its mechanical impedance dynamically within each gait cycle and across

[1] A detailed review of human gait biomechanics is provided in Appendix A

various gait schemes (Au, *et al.*, 2008), passive prosthetics lack adaptability to the user, the gait scheme, and the environment (Voloshina, and Collins, 2019).

In these respects, active prosthetic devices have shown promise, with studies reporting reductions in metabolic cost and increases in walking speeds (Voloshina, and Collins, 2019). These improvements can be attributed to the active power modulation (and thereby intra-gait cycle power injection). The development of purely active ankle prostheses is, however, hindered by significant engineering challenges. Current actuator technologies lack the requisite torque and power densities to achieve appropriate rehabilitation (Au, *et al.*, 2008; Gao, *et al.*, 2018). To overcome these torque and power limitations, passive elements are frequently used in parallel or series with active actuator elements. Common designs utilize ball screws (either direct-drive or timing belt-driven) with parallel or series passive springs.

Most research involving passive element design targets energy storage during the Controlled Dorsiflexion (CD) gait phase and its release during the Powered Plantarflexion (PP) phase to economize power consumption during walking. Hence, most devices have either fixed cantilever or coil springs (Au, S. K., *et al.*, 2007; Bellman, *et al.*, 2008; Hitt, *et al.*, 2007; Sup, *et al.*, 2008), or a cam-based design (Gao, *et al.*, 2018) that mimic the biological elastic response of the human ankle. These designs feature fixed stiffness and equilibrium angles[2] specifically fine-tuned for walking. This, however, imposes severe limitations on the user's ability to perform other activities including stair ascent/descent, ramp up and ramp down, and sit-to-stand transitions.

[2] Passive elements are typically implemented with on-off mechanical characteristics. The equilibrium angle is the angle at which the spring connects to the ankle foot-complex in the direction of dorsiflexion. For walking, although the equilibrium angle is -5°, most designs use 0° to economize power requirements during standing.

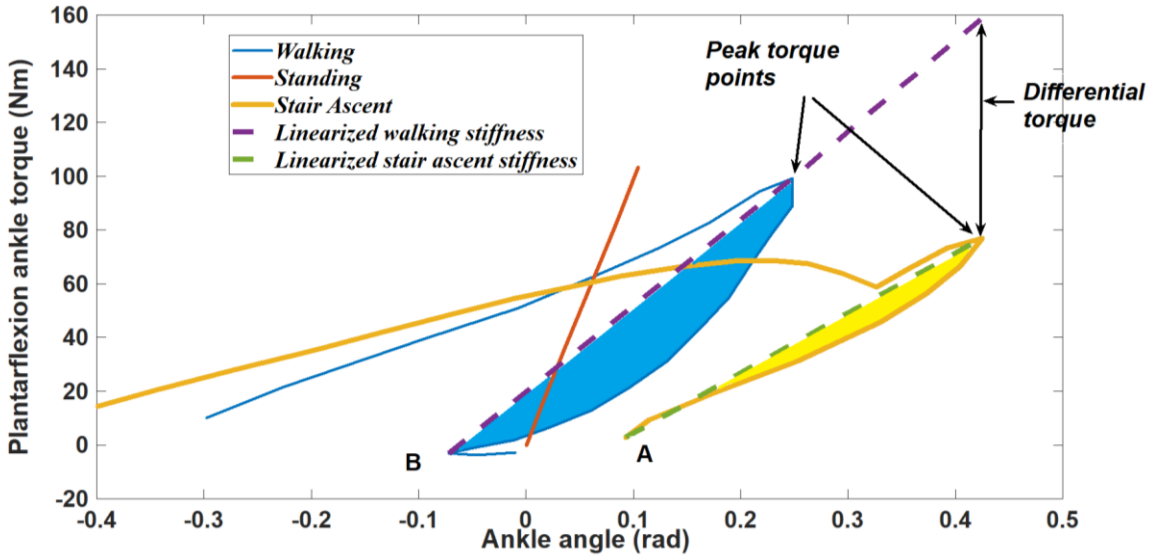


**Figure 1. 1** Ankle torque-angle curves for a 75 kg able-bodied individual for various gaits, adapted from Shepherd, and Rouse, 2017. A and B are equilibrium points for stair ascent and walking, respectively. Linearized CD ankle stiffness curves typically provide the passive spring stiffness values for walking and stair ascent (the linear spring is typically designed to achieve the equilibrium angle-to-peak torque point torque-angle trajectory). The shaded regions, yellow and blue, show the required additional actuator torque for stair ascent and walking, respectively. The designated differential torque indicates the actuator torque required for achieving the peak required stair ascent torque when using a spring fine-tuned for walking.

As an example, consider the ankle torque-angle curves for a 75 kg able-bodied individual shown in Figure 1.1. The ankle must modulate its stiffness to achieve the stair ascent and walking torque-angle curves (yellow and blue curves shown in Figure 1.1) for a stable gait. Here, using a linear passive spring (linear from the equilibrium point to the peak torque point: the linearized Controlled Dorsiflexion curves) with angular stiffness and equilibrium angle values of 223.23 Nm/rad and 0.093 rad (5.32$^{o}$) for stair ascent and 319.61 Nm/rad and -0.072 rad (-4.13$^{o}$) significantly reduces the actuator torque requirements (shaded zones in Figure 1.1). Figure 1.1 reveals that for a spring fine-tuned for walking, the actuator may have to supply a torque in excess

of its rated capacity (the differential torque of 82 Nm exceeds the typical actuator capacity of 45-50 Nm) and therefore be infeasible.

A consequence of this design strategy is that most active prosthetic devices have constricted ranges of motion. Some semi-active devices have overcome this issue partially, by means of electrically-modulated spring mechanisms (Glanzer, and Adamczyk, 2018; Shepherd, and Rouse, 2017) which varies the spring stiffness (but not its equilibrium angle). Such systems typically lack an active power element due to weight considerations.

For active devices, direct-drive ball screw designs utilize a commercially available motor. This motor is then coupled to a ball screw with a parallel mechanical structure to bear the ball screw load (Bellman, *et al.*, 2008; Hitt, *et al.*, 2007; Sup, *et al.*, 2008). This causes a significant increase in the length and weight of the actuator. Alternately, timing belt-driven ball screw designs (Au, *et al.*, 2007; Au, *et al.*, 2008; Gao, *et al.*, 2018) can suffer from assembly and maintenance issues.

In this thesis, we introduce the *VSeM Ankle (**V**ariable **S**pring **em**bedded **M**otor-ball screw **Ankle**)*, an active ankle prosthesis with novel features in both the actuator and passive elements. The spring mechanism features high offline stiffness and equilibrium angle manipulability, achieved via a slider-crank mechanism incorporating Belleville springs. The desired variation in stiffness and equilibrium angle can be easily achieved by altering the spring stack configuration. Furthermore, to overcome the size and weight limitations of direct-drive ball screw designs and the assembly and maintenance limitations of timing belt-driven designs, a novel embedded ball screw design is presented which achieves a significant reduction in actuator length and obviates the need for timing belts.

### 1.3 Design requirements and desired outcomes

The design is optimized for a human weight of 75 kg (due to the widespread availability of associated literature) resulting in torque requirements of approximately 120 Nm for walking, as inferred from Figure A.4 (in Appendix A). Furthermore, most common gait schemes such as walking, stair ascent, and stair descent have a required range of motion of 30-50º (Azocar, *et al.*, 2018; Shepherd, and Rouse, 2017) and hence, the lower limit of the desired range of motion (ROM) is set to $50^{o}$. Finally, the height and mass specifications are set to 23.0 cm and 2.5 kg, respectively, based on specifications for commercially available prostheses and average human ankle-shank weight (Au, *et al.*, 2007). The design strategy flow chart for this work is provided in Appendix B. Furthermore, additional desired characteristics (to be assessed experimentally) are a motion bandwidth greater than 2 Hz (Satkunskiene, *et al.*, 2009), ankle torque (exerted by the actuator) bandwidth which is at least 0.5 Hz (for slow walking), and a manually achievable device backdrivability (Elery, *et al.*, 2018).

### 1.4 Scope of the study

After establishing the design requirements and methodology, this thesis details the mechanism and actuator design. Next, the spring mechanism design is presented, followed by structural design and optimization. Finally, an impedance controller is devised, followed by experimental testing of device bandwidth, inherent mechanical impedance, spring characteristics, and impedance controller response.

# CHAPTER 2. METHODS

## 2.1 Actuation mechanism and transmission design and construction

The actuation mechanism is the most critical element of the *VSeM Ankle* prosthesis; its design is governed by the required ankle torque and velocity, device weight, and height, as discussed in Section 1.3. This section commences with a brief explanation of the prototype mechanism and continues with an overview of device kinematics, followed by a discussion of the transmission design. Finally, the construction of the prototype actuator is explained in detail.

### 2.1.1 Actuation mechanism

The actuator design, detailed in Figure 2.1, utilizes a four-bar linkage mechanism, which provides significant torque density with limited size and mass (Azocar, *et al.*, 2018). This actuator consists of an embedded motor, fixed to the support frame by revolute joint D. This motor drives a ball screw, with ball nut hinge-connected at B to the foot-crank. The foot-crank complex (crank fixed to the prosthetic foot) forms a revolute joint at A (the ankle joint) with the support frame and clevis. Hence, as the motor rotates the ball screw, the distance between the B and D changes, causing rotation of the foot-crank about the ankle joint (A). The support frame is fixed to the amputee's residual limb via a pylon: an aluminum rod with pyramid connectors on both ends. The distal pyramid connector interfaces with an adapter fixed to the support frame. The passive element (spring) and its design are discussed in detail in section 2.4.

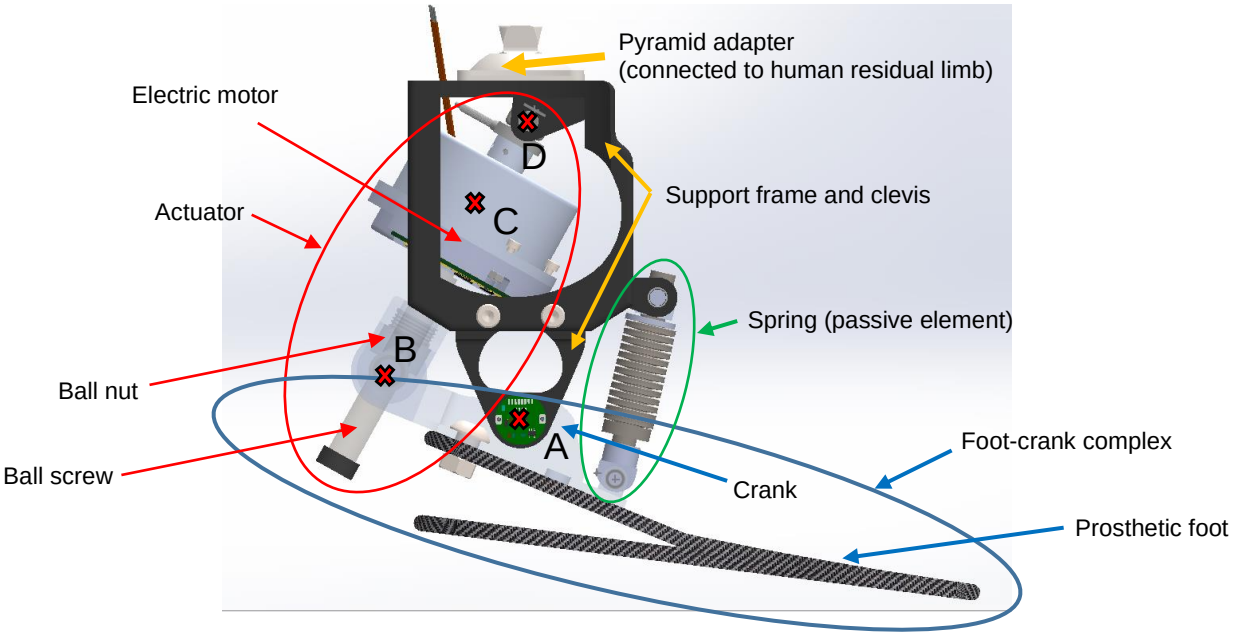


**Figure 2.1** Side view of the actuated prosthetic ankle prototype, showing linkage components with the motorized actuator (red), prosthetic foot-crank complex (blue), and spring (green). Joints A, B, C, and D represent the ankle joint, crank-actuator revolute joint, stator-rotor rotary joint (with rotation about the actuator's length axis), and motorized actuator-support frame revolute joint, respectively (located by crosses). The support structures are indicated by yellow arrows.

### 2.1.2 Mechanism kinematics

The prosthetic ankle system of Figure 2.2 can be modeled by defining appropriate kinematic variables: $\tau_a \; and \; \tau_m$ represent the ankle and motor torques, respectively ($Nm$); $L_{AB}$ is the length of crank AB ($m$); $\alpha$ is the crank angle (with respect to the vertical, *rad*). The relation between crank angle ($\alpha$) and ankle angle ($\theta$) is given by $\theta = \alpha - 73°$ since the slope of the prosthetic foot-crank interface is -17° with the horizontal. $\delta$ is the angle made by the link BD with the vertical axis as shown in the schematic; it is positive for clockwise rotations about the vertical axis. $L_{BD}$ is the length of the electric actuator, i.e. the distance from the mounting point D to the connecting point B. $L_{ADy}$ is the vertical component of the distance between the ankle joint A and the actuator mounting point D; $L_{ADx}$ is the horizontal component of this distance. $\gamma$ is the angle of rotation of the electric actuator rotor which is set to 0º for $\alpha$= 73° i.e. about the zero-ankle angle position (equilibrium angle).

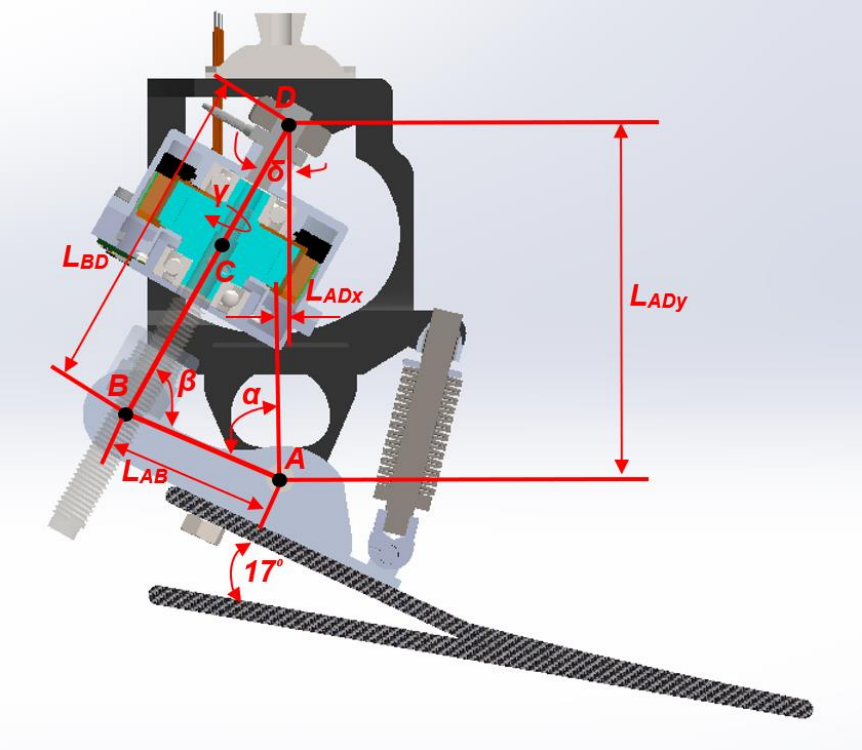


**Figure 2.2** Linkage diagram of the device (spring linkage notations not shown). A, B, C, D are the specific points of interest in the linkage with related angles *α, β, γ, δ* respectively.

Based on these variables, kinematic relationships can be sequentially derived:

$$L_{AB}\,sin(\alpha) + L_{ADx} = \{L_{ADy} - L_{AB}\,cos(\alpha)\}\,tan(\delta) \tag{1}$$

$$\delta = tan^{-1}\frac{L_{AB}\ sin(\alpha) + L_{ADx}}{L_{ADy} - L_{AB}\,cos(\alpha)} \tag{2}$$

$$L_{BD} = \frac{L_{ADy} - L_{AB}\,cos\,\alpha}{cos\,\delta} \tag{3}$$

Because the ball screw is directly mounted to the rotor, the number of rotations of the ball screw equals the number of motor rotations; the ball screw rotations can be computed using the change in the length of the electric actuator $L_{BD}$. Hence rotor angle γ can be computed by solving

$$\Delta L_{BD} = \gamma\frac{p}{2\pi} \tag{4}$$

where $\Delta L_{BD} = L_{BD} - L_{BD,\ \theta=0}$ and $p$ = 2 mm is the pitch of the ball screw.

However, to facilitate controller synthesis, kinematic relationships for δ, γ (in terms of θ) can be obtained by second-order regression as follows:

$$\delta = -0.154\theta^2 - 0.1055\theta + 0.5548 \qquad (R^2 = 0.997) \tag{5}$$

$$\gamma = -23.476\theta^2 + 164.15\theta + 0.2668 \qquad (R^2 = 0.9982) \tag{6}$$

Two important design considerations are the required motor velocity ($\dot{\gamma}$) and ankle torque ($\tau_a$); these values can be derived from (1-4):

$$\dot{\gamma} = \frac{2.\pi}{p}\dot{\theta}\, L_{BD}\, \{cos(\alpha)\, sin(\delta) + sin(\alpha)\, cos(\delta)\} \tag{7}$$

$$\tau_a = \tau_m\, \frac{2.\pi}{p}\, L_{AB}\, cos(\alpha + \delta) \tag{8}$$

To initiate the design parameters, an optimization routine was implemented in MS Excel using the GRG non-linear solver. The objective function was the planar area of the 4-bar linkage mechanism and the constraints were constructed from the design requirements specified in Section 1.3: $L_{ADy} < 0.18$ m (because the nominal ankle joint to ground distance is assumed to be 5 cm, and the allowable height of the device is 23 cm, hence 23-5=18cm), $L_{AB} < 0.1$ (an initial guess), $L_{ADy} - L_{AB} > 0.05$ (the motor is assumed to have an initial length of 5 cm), and the maximum ankle torque ≥ 120 Nm. Three remaining design parameters ($L_{ADx}$, motor torque capacity $T_m$, and ball screw pitch $p$) were derived from literature. The initialized design parameters are compiled in Table 2.1.

**Table 2.1** Optimized initial kinematic parameter values

| **Parameter** | $L_{AB}$ (m) | $L_{ADy}$ (m) | $L_{ADx}$ (m) | $T_m$ (Nm) | $p$ (m) |
|---|---|---|---|---|---|
| **Value** | 0.056 | 0.115 | 0 | 0.81 | 0.002 |

### 2.1.3 Design and fabrication of the transmission

As discussed in the Introduction (Section 1), a direct-drive ball screw transmission was chosen to provide compact power transfer with minimal maintenance. Although most comparable transmissions utilize a commercial motor coupled to a ball screw with a parallel mechanical structure to bear the ball screw load (Hitt, *et al.*, 2007; Sup, *et al.*, 2008), this significantly increases the length and weight of the actuator. Hence, a novel motor embedded ball screw design was developed to overcome the above issues. To achieve this, an extensive evaluation of commercially-available frameless motor kits was conducted based on high torque density and design flexibility. The selected motor kit from Celera Motion, MA (Celera Motion model UTH-63-B-18-C-x-000) (shown in Figure 2.3) provided 0.268 Nm of rated torque with a total mass of 300 grams.

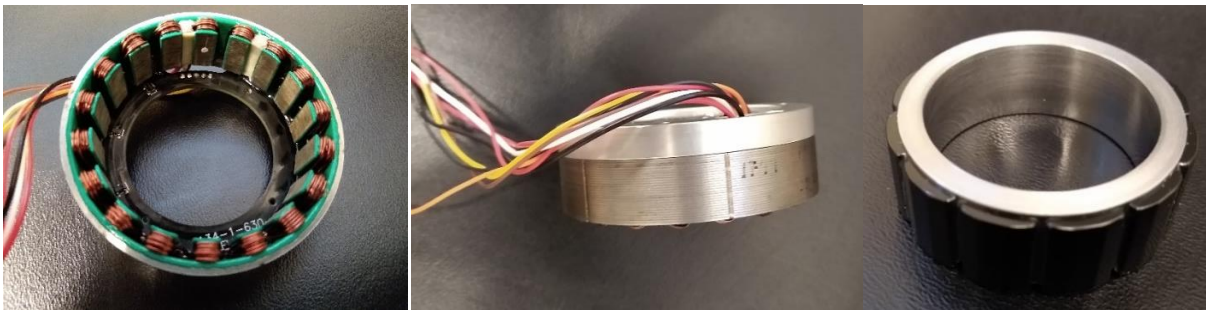

(a) (b) (c)

**Figure 2.3** Photographs of the Celera motor kit: (a) Stator interior showing poles, windings, and Hall effect sensors (black ring); (b) Stator exterior showing laminations and wiring; (c) Rotor view showing NdFeB magnets and back iron.

As can be seen in Figure 2.3(c), the rotor has a cylindrical mounting cavity, enabling a ball screw to be readily embedded into the rotor hub. An SKF Motion ball screw with a 2 mm pitch (SKF model SD 12x2R 82_125_G7_L-Z_WPR) was selected based on force, velocity, and mounting considerations. To assess the effectiveness of the transmission (from the motor to foot-

crank), ankle torque-velocity and power-velocity simulations were performed using the brushless DC (BLDC) motor model as modeled by Malzahn, *et al.*, 2017:

$$\dot{\gamma} = \frac{V}{k_t} - \frac{R \cdot}{{k_t}^2} \tau_m \tag{9}$$

where $V$ is the motor voltage, $k_t$ is the motor torque constant (Nm/Amp), $R$ is the motor's electrical resistance (ohms), and $\tau_m$ is motor torque (transferred from the ball nut to the ball screw). When used in conjunction with the kinematic equations (1-4, 7-8), this model can be used to compare the prosthetic ankle's performance to available able-bodied individual data (Gates, 2004), as shown in Figure 2.4. It must be noted that these curves are theoretical curves which assume steady-state conditions and perfect cooling. In practice, the heat dissipation from the stator, and transient torque and velocity behaviors significantly reduce the real torque and power capacities. Hence, as shown in (Au, *et al.*, 2007), a safety margin is maintained. The parameters used in the simulation (and the final values) are given in Table 2.2.

**Table 2.2** Final linkage and electromechanical parameters

| **Parameter** | $L_{AB}$ (m) | $L_{ADy}$ (m) | $L_{ADx}$ (m) | $V$ (V) | $k_t$ (Nm/A) | $R$ (Ω) |
|---|---|---|---|---|---|---|
| **Value** | 0.055 | 0.117 | 0.0031 | 30 | 0.028 | 0.26 |

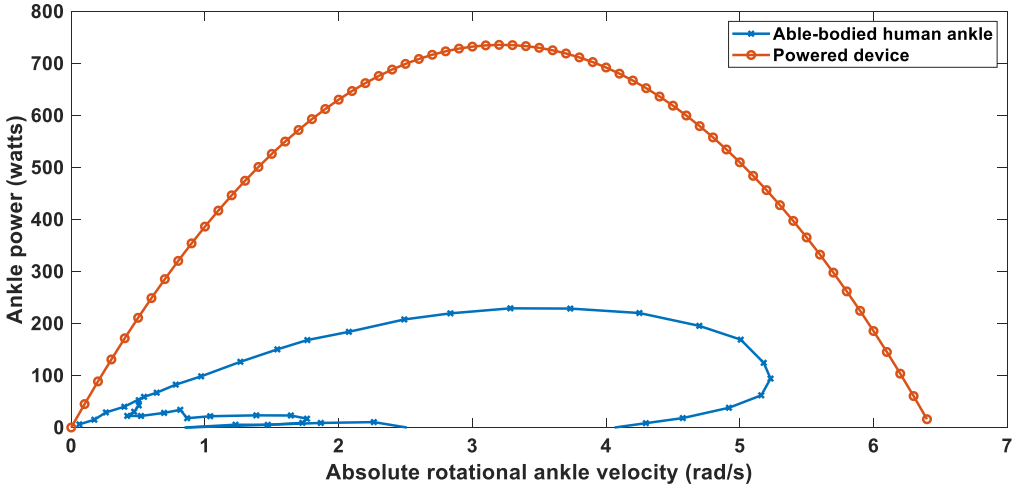


**(a)**

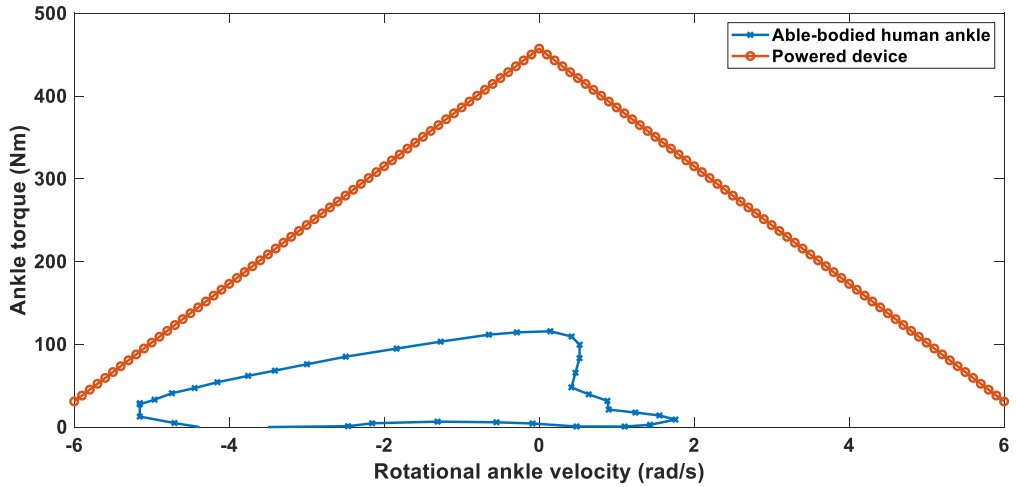


**(b)**

**Figure 2.4 (a)** Ankle power – velocity simulation curves for able-bodied human ankle and powered actuator ankle **(b)** Ankle torque – velocity simulation curves for able-bodied human ankle and powered actuator ankle

Figure 2.4 reveals that for all the required angular velocities, the ankle torque and power supplied by the powered device are greater than the required human ankle torque and power, respectively. Hence, it can be inferred that the transmission system is feasible.

The next step involved detailed actuator design and construction. Consider the motor and actuator construction shown in Figures 2.5 and 2.6. The stator housing and lower shell (with the mounted encoder chip) are fastened together, while the stator (with the Hall sensing board) is glued to the stator housing via epoxy adhesives. The load cell and motor pin are joined using inserts; this sub-assembly is then threaded (and secured with inserts) to the stator housing to form the 'stator system'. The rotor (with the embedded ball screw and connector), the encoder ring, and the encoder mount form a 'rotor system' sub-assembly, as shown in Figures 2.5 and 2.6. The 'stator and rotor systems' are connected structurally via two angular contact bearings, forming a rotational joint (referred to previously as 'C').

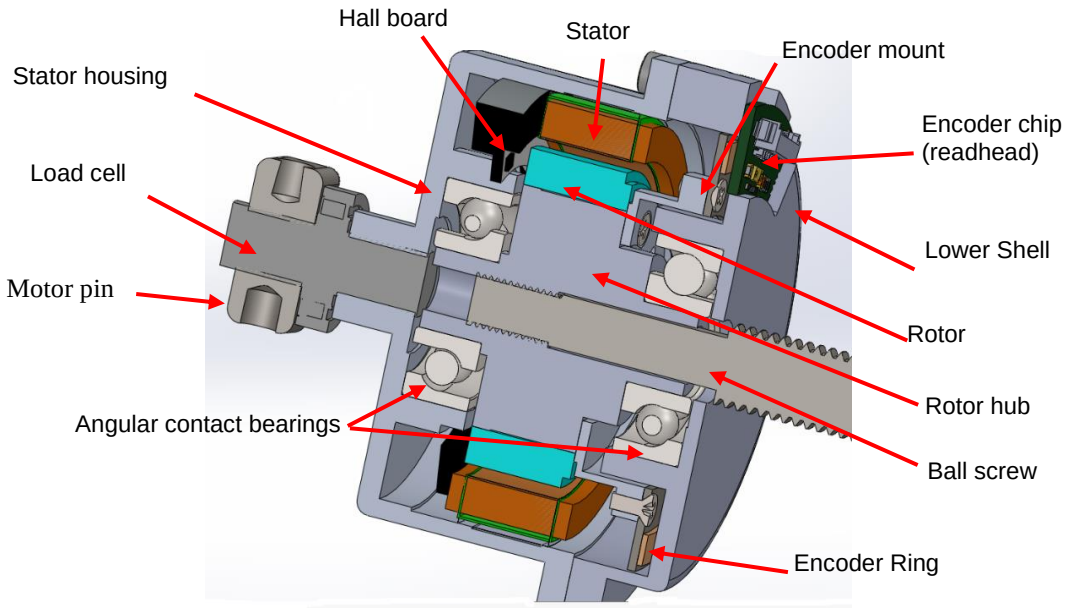


**Figure 2.5** Cross-sectional view of the actuator with the principal internal components shown.


**Figure 2.6** External photograph of the fabricated actuator. The ball nut and connector form a threaded joint and the motor pin mounting connects the motor pin to the support frame to form a revolute joint 'D'.

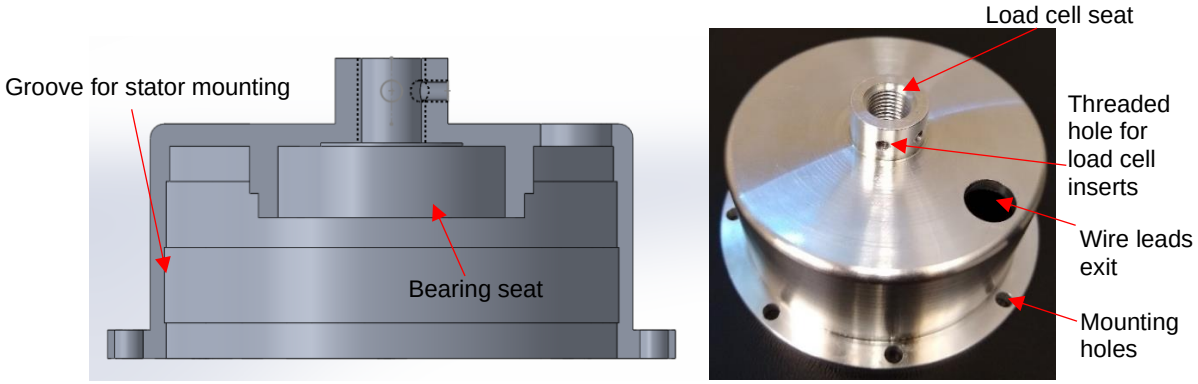


**Figure. 2.7** Stator housing construction. CAD model of stator housing (left) shows internal mounting details. Actual stator housing (right) shows the essential functional and mounting aspects.

The stator housing (as shown in Figure 2.7) was designed based on guidelines provided by Celera Motion (Celera Motion 2018). The stator housing was machined from Al 7075-T7351 (due to its superior mechanical properties) using a CNC lathe and drilling machine. The stator was secured to the stator housing via a 3M DP420M structural epoxy adhesive applied to a 0.01" groove in the stator housing (shown in Figure 2.7) and to the stator's laminated stacks. This assembly (shown in Figure 2.8) was cured at room temperature (73 ºF) for 24 hours as recommended by the epoxy manufacturer. A threaded seat for the axial load cell along with threaded holes for gripping inserts was designed into the housing. Furthermore, a small circular hole was machined to allow for routing of the wire leads.

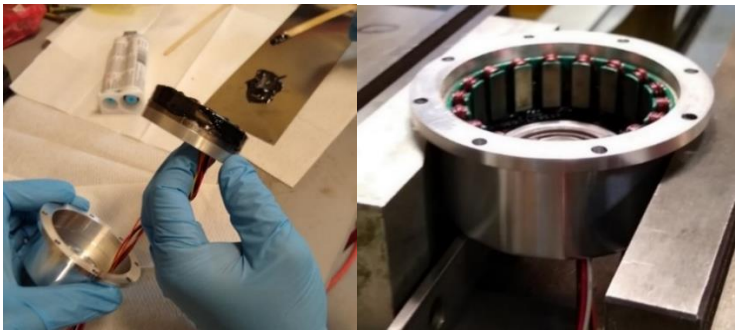

(a) (b)

**Figure 2.8 (a)** Application of the epoxy adhesive on the stator **(b)** Final assembled stator in housing

The lower shell (shown in Figure 2.9) and rotor hub (Figure 2.10) were similarly machined from Al 7075-T7351. The cut on the lower shell was specifically designed to mount the motor encoder chip via four M2.2 screws. The bearing seats are designed for the angular contact ball bearings (SKF 7201). The magnetic rotor was glued to the rotor hub using 3M DP420 epoxy adhesive and was cured at room temperature (73 ºF) for 24 hrs.

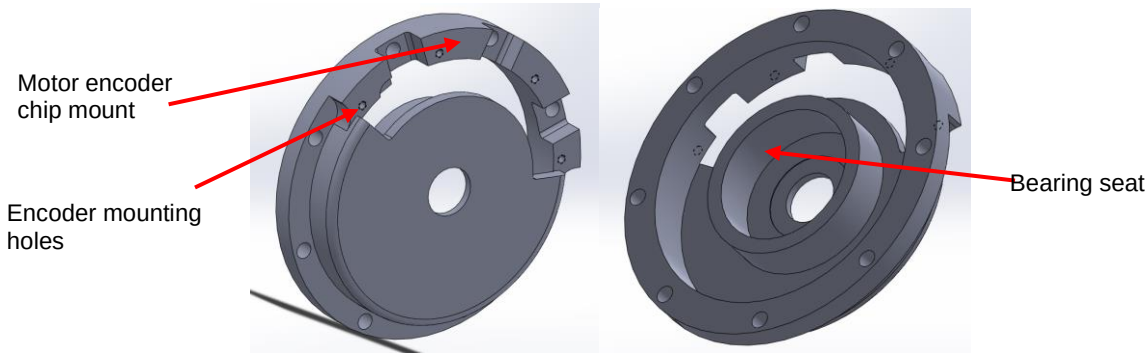


**Figure 2.9** Lower shell details. The external view i.e. visible from outside the motor (left) and internal view (right).

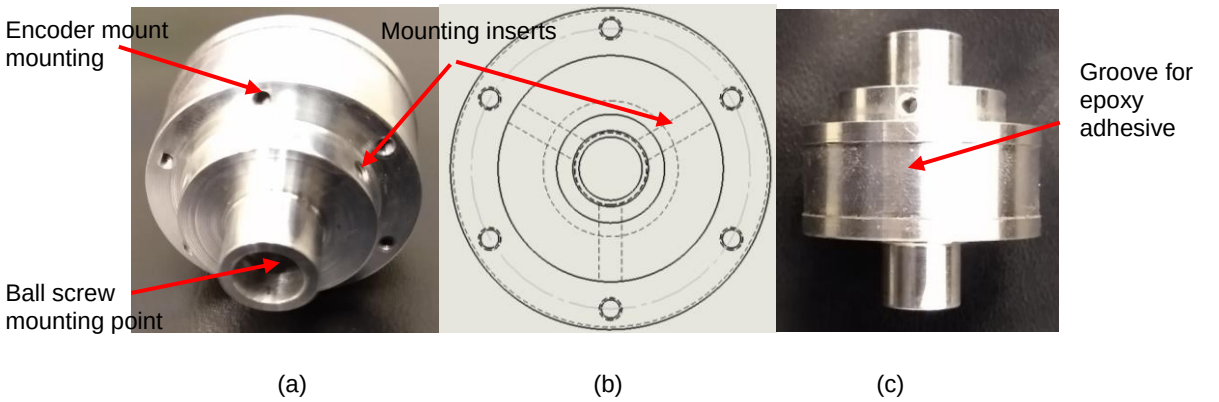


**Figure 2.10** Mounting points on the rotor hub **(a)** actual rotor front view **(b)** rotor 2D drawing view **(c)** top view of the rotor hub

The ball screw was mounted (after initial motor construction without the ball screw, shown in Figure 2.12) by a threaded joint (M8x1) inside the rotor hub to bear and transmit the axial load. Furthermore, 3 inserts (shown in Figure 2.10) were used to radially secure the ball screw. It is important to note that using three inserts is essential for both holding power/torque and finer positioning of the ball screw.

For initial motor assembly and testing, the rotor and stator assemblies were assembled using a CNC milling machine (any other machine which can lower the rotor while holding the stator can be used here) to avoid damage to rotor magnets due to high magnetic forces as shown in Figure 2.11 (b). As can be seen in Figure 2.10 and Figure 2.11, the rotor has 6 M2.2 holes for mounting an encoder mount, on which is then mounted the magnetic encoder ring using 8 M2.2 screws (shown in Figure 2.12a), which is also made from Al 7075-T7351 and CNC machined. The initial motor tests were conducted using the support frame as a fixture as shown in Figure 2.12.b.

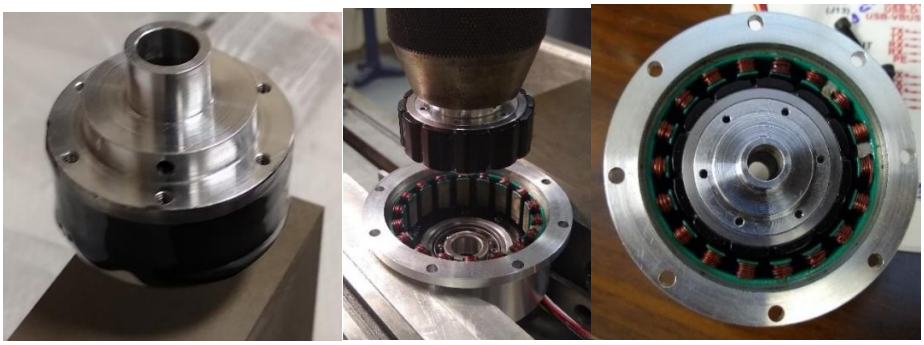

(a) (b) (c)

**Figure 2.11 (a)** Epoxy coated Rotor hub **(b)** Stator and rotor being assembled using CNC milling machine **(c)** Final stator-rotor assembly

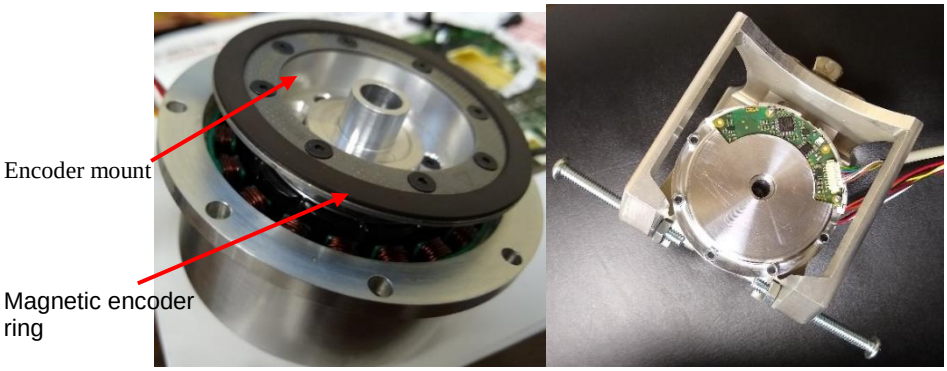


(a) (b)

**Figure 2.12 (a)** Encoder ring mounted on the rotor before complete assembly **(b)** Motor assembly (without the ball screw) for initial testing using the support frame with two M6 bolt-nut assemblies as a fixture.

After the initial motor tests, the ball screw was mounted onto the rotor, as described earlier. Next, the ball nut was mounted directly to the connector (Al 7075-T7351) via a threaded M18x1 hole as shown in Figure 2.6; this acts as the point of force interaction between the crank and the ball screw. Finally, a Futek inline load cell (Futek Model FSH03905) was selected for its load capacity and external torque holding capacity and was embedded on the stator housing to measure the force along the actuator length. A part named ‘motor pin’ (shown in Figure 2.5 and 2.6) was manufactured from AISI 4140 (for higher strength) with a 3/8-24 threaded hole for mounting the

load cell along one axis and two 1/4-28 threaded holes on a perpendicular axis for mounting on the support frame.

## 2.2 Design of passive element

Utilizing the optimal passive element (spring mechanism) is important to achieving significant reductions in required motor torque (and thereby lower heat dissipation), power, and overall weight in a lower-limb prosthetic. Specific key aspects of this passive element design process include achieving required angular stiffness, which varies across different gait schemes and patients of differing weight and height, and angle of engagement (i.e. equilibrium angle). Hence, it is essential to design a passive element that provides adaptability in both angular stiffness and equilibrium angle. For these reasons, Belleville springs in a slider-crank mechanism were employed. Belleville springs (Figure 2.13) are essentially conical rings made of spring steel with trapezoidal cross-sections to provide uniform stress distributions; they are ideally suited to space-limited applications. Their principal advantage, in the context of this work, is the versatility of various parallel stack configurations. Hence, the use of Belleville springs and hardened washers (for stack height adjustment) enables the desired passive element properties of angular stiffness and equilibrium angle to be achieved.

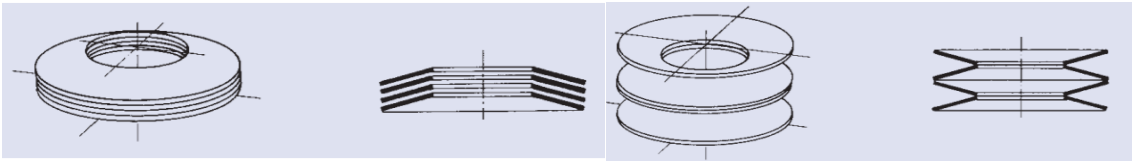

(a) (b)

**Figure 2.13** Belleville spring stack **(a)** in parallel **(b)** in series

The passive element was designed by incorporating Belleville springs into a slider-crank mechanism, as shown in Figure 2.14. This mechanism involves a series spring stack mounted on a steel piston rod (A2 Steel, HRC 38), with the rod forming a prismatic joint at the upper spring mounting bracket (7075-T7351 grade aluminum), which has a sleeve bearing and is mounted via a press fit.

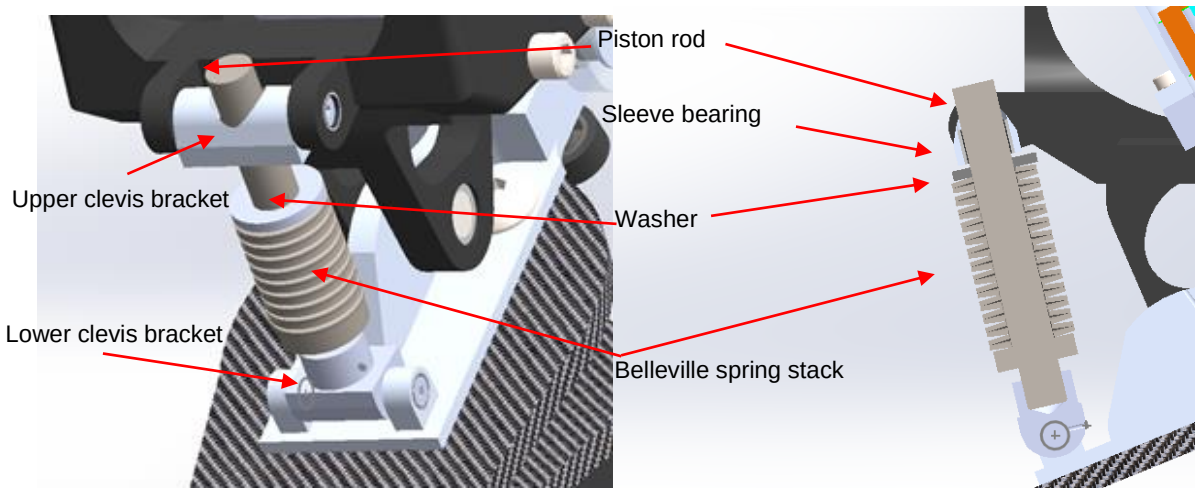


**Figure 2.14** Frontal (left) and side section (right) views of the spring element (differing spring configurations are shown to clarify modular functionality)

The upper spring mounting bracket forms a revolute joint at the two hinges on the support frame as shown. The other end of the piston rod is threaded to the lower spring mounting bracket (7075-T7351 grade aluminum) which is pin-connected to a crank to form a revolute joint. A hardened steel lock-washer (with HRC 51) is located at the stack end near the upper spring mounting bracket to protect the bracket from damage due to indentation by the springs. This is an important structural consideration since Belleville springs tend to have hardness values in the range of HRC 50-60. Hence, the hardened washer's hardness must lie in the vicinity (±5 HRC recommended by spring manufacturer).

Kinematic modeling of the spring mechanism was conducted to study spring engagement during the Controlled Dorsiflexion (CD) and Powered Plantarflexion (PP) phases for ankle angles greater than the set equilibrium angle ($\theta_o$). This kinematic modeling approach utilized the design variables shown in Figure 2.15.

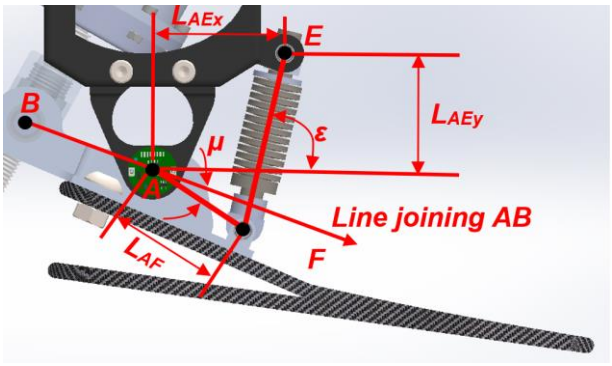


**Figure 2.15** Dimensional representation of the spring and its principal spatial parameters.

Using these spatial parameters, the following kinematic relations can be sequentially derived.

$$L_{EF} = \sqrt{(L_{AEx} - L_{AF}\, cos(\mu + 17^0 - \theta))^2 + \left(L_{AEy} + L_{AF}\, sin(\mu + 17^0 - \theta)\right)^2} \quad (10)$$

$$\Delta L_{EF} = (L_{EF})_{\theta_o} - L_{EF} \quad (11)$$

$$F_s = k \times \Delta L_{EF} \quad (12)$$

$$\varepsilon = tan^{-1} \frac{L_{AEy} + L_{AF}\, sin(\mu + 17^0 - \theta)}{L_{AEx} - L_{AF}\, cos(\mu + 17^0 - \theta)} \quad (13)$$

The spring torque is hence given by:

$$\tau_{spring} = L_{AF}\, F_s\, cos(\varepsilon - \alpha) \quad (14)$$

where $\mu$ is the angle between the crank link and the line connecting the spring mounting on foot to the ankle joint, $k$ is the linear stiffness of the spring given in N/mm.

The spatial parameters of the mechanism were derived from an iterative design strategy using CAD modeling (SolidWorks) in conjunction with torque-angle specifications derived from an actuator-spring linkage model. The requisite stiffness ($k$=196.34 N/mm and $\theta_o$ = 0 rad) is achieved using 23 Belleville springs in series, as shown in Figure 2.16. A quadratic regression to this data ($\tau_{spring} = -128.81\,\theta^2 + 403.33\theta - 0.9348$) results in $R^2 = 0.9997$.

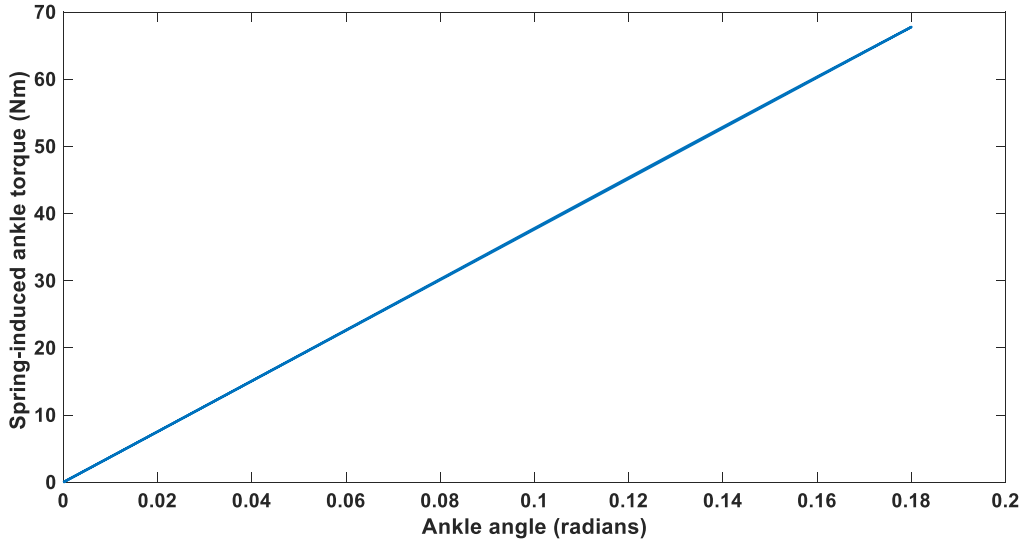


**Figure 2.16** Simulated spring torque – ankle angle chart for current spring configuration using linear stiffness $k$=196.34 N/mm and equilibrium angle $\theta_0$ = 0 rad.

The spring selection depends on two specific parameters: the required angular stiffness of the passive element (linked to linear stiffness of stack) and the equilibrium angle (linked to stack height). The angular stiffness and equilibrium values are obtained from the ankle torque-angle curve for each specific gait scheme (commonly walking) as discussed in Appendix A. Based on able-bodied human biomechanics for walking, the equilibrium angle is approximately -0.12 rad. But as a power economy tradeoff between standing and walking, the desired equilibrium angle

was set to 0 rad (a -0.12 rad equilibrium implies that the motor needs to supply torque when the patient stands at 0 rad ankle angle). Hence, different stack stiffness values were considered with the configurations relying on the mechanical properties of commercially available springs. The current configuration was derived with the condition that the peak load torque should be approximately equal to the rated motor torque (0.268 Nm) for a reduction in heat dissipation, for which $k$=196.34 N/mm and equilibrium angle $\theta_o$ = 0 rad using the aforementioned 23 Belleville springs and one wedge lock washer) yields the desired outcome. This can be seen in Figure 2.17, which plots the required motor torques with and without the specified spring configuration.

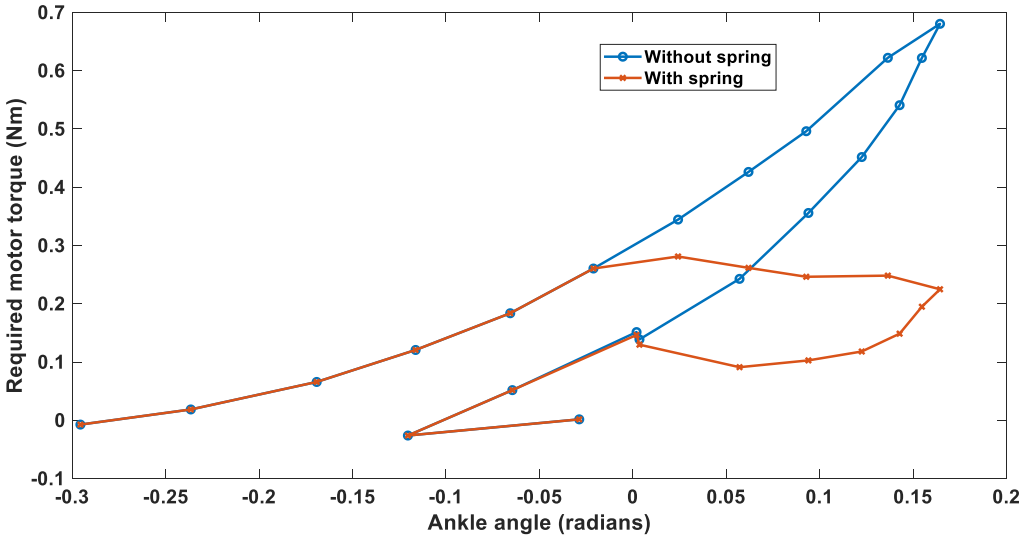


**Figure 2.17** Comparative plot of required motor torque for walking (75 kg able-bodied individual) with and without the spring element (linear stiffness $k$=196 N/mm and equilibrium angle $\theta_o$ = 0 rad). The plot was derived using a combined actuator-spring model which is based on the kinematic models for the actuated mechanism and spring element.

## 2.3 Structural design

The structural design followed an iterative design strategy that was constrained by the peak torque (120 Nm peak), maximum height (< 23 cm), and maximum mass (< 2.5 kg) requirements. This structural design was initiated using the parameters derived from the actuator and linkage development optimization (presented in Section 2.1.2). The assembly and part designs were then

iteratively updated via the 3D CAD modeling software (SolidWorks), which helped inform subsequent actuator and linkage design by providing a visual framework. Concurrent to the 3D modeling, device torque characteristics were evaluated via a combined actuator-spring model (based on the kinematic models for the actuated mechanism and spring element). The design iterations were terminated after a 3D CAD assembly meeting all requirements was obtained. Figure 2.18 shows the principal components of the optimized structural design.

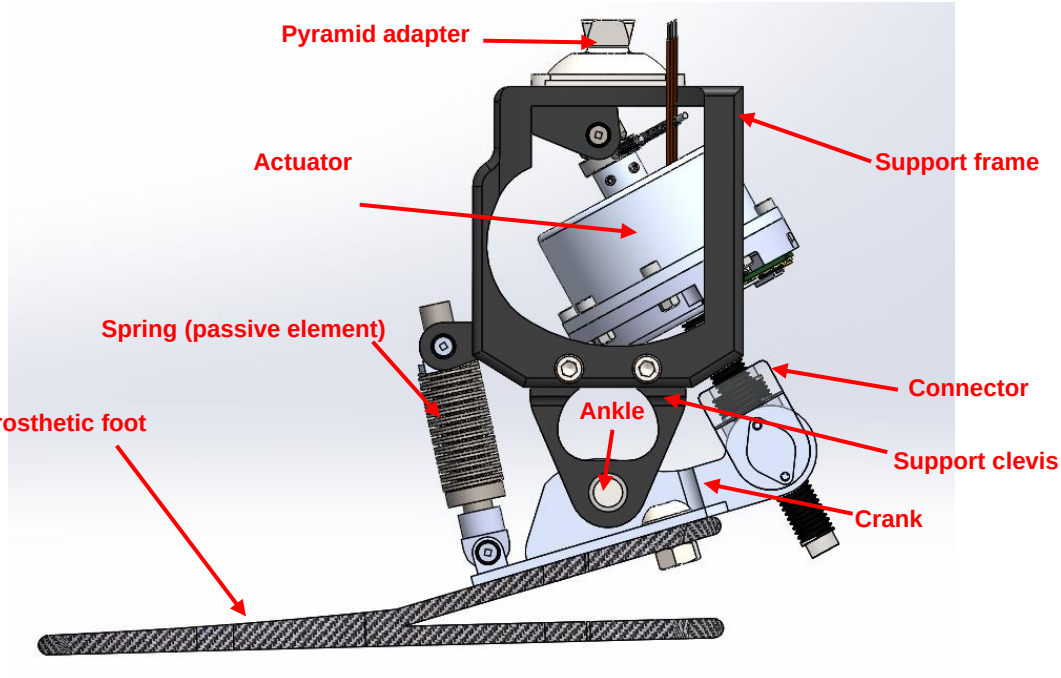


**Figure 2.18** Structural description of the *VSeM Ankle* with the principal components captioned

The support frame and support clevis were manufactured from aluminum (grades 7075-T6 and 7075-T7351, respectively) for superior strength and weight while the manufacturing was conducted via wire electric discharge machining (EDM) and milling operations. These components were separated to facilitate machining and are then fastened together using four 1/4-28 bolts. The pyramid adapter is fastened to the support frame by four M6 bolts. This pyramid

adapter can be connected to a pylon which can then be connected to the residual human limb socket. Finally, a carbon-fiber prosthetic foot from Ossur (LP-Variflex foot) was selected based on its superior energy and shock absorption characteristics. The foot was fastened to the crank (part of the linkage) via two 3/8-24 nut-bolt assemblies (the necessary holes were machined via water jet cutting).

The actuator is mounted to the support frame using two 1/4-28 partially threaded bolts; its other end is secured to the crank using two 3/8" pins, forming 2 revolute joints. The spring mechanism is mounted to the support frame via two 1/4-28 partially threaded bolts; its other end is secured to the crank by a single pin, forming a revolute joint. The crank was machined from aluminum (grade 7075-T7351). The resulting single DOF device pivots about the ankle, as shown in Figure 2.18. The crank and support clevis are mounted together at the ankle, forming a revolute joint via a steel pin. The spring stack and a crank edge provide the requisite mechanical stiffness and hard stops. The resulting range of motion of the system is 55º or 0.96 rad (30º or 0.52 rad dorsiflexion and 25º or 0.44 rad plantarflexion). The prototype mass was 1.9 kg excluding electronics.

To assess the structural feasibility of the designed parts, finite element analysis was conducted on the principal structural components namely: the support frame, support clevis, and the crank. The factor of safety for this design was set at 3.0 based on existing literature (Azocar, 2018). Based on yield strengths of 435 MPa and 503 MPa for aluminum grades 7075-T7351 and Al 7076-T6, respectively (ASM Handbook Committee, 1990), this limits von Mises stresses to 145 and 167.67 MPa, respectively. A finite element analysis (FEA) study of the design was conducted using ANSYS Workbench (Ansys Inc, Canonsburg PA) and implemented using an adaptive mesh. The required forces and constraints were based on the torque parameters for a 75

kg able-bodied individual, and the device structure at an ankle angle of 0.15 rad (the limiting case i.e. peak torque of 120 Nm at controlled dorsiflexion). The resulting stress distributions for the crank and support clevis are shown in Figure 2.19.

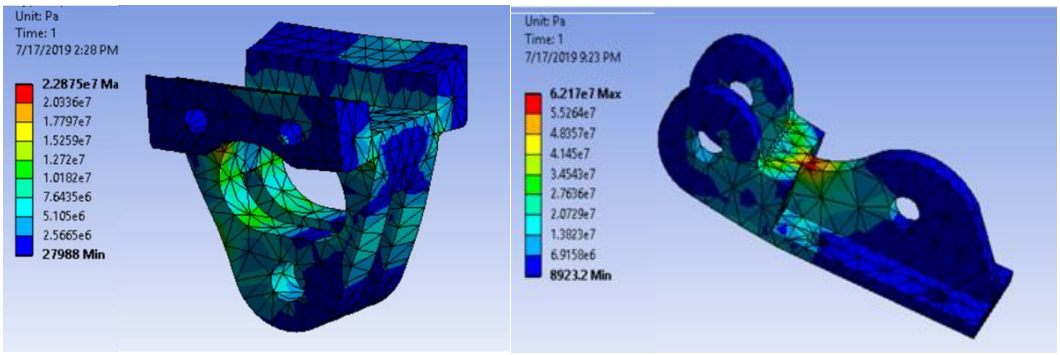


(a) (b)

**Figure 2.19** Simulated von Mises stress distributions for the peak torque condition at $\theta = 0.15$ rad based on the biomechanical data from an able-bodied 75 kg able-bodied individual (Gates, 2004) of (a) Support clevis (b) Crank

The support frame, being the largest structural component, required special attention. To inform the design of the support frame, a compliance minimization based topological optimization was conducted in ANSYS Workbench with the following design constraints: optimized mass lower limit was set to 50% of the original pre-optimization mass for each iteration (initial part iterations showed extreme mass reductions for constraint limits below 50%, owing to excess mass distributions in initial part designs, resulting in unmanufacturable parts) and peak global von Mises stress was set to 167.67 MPa (derived from the yield strength of 503 MPa for 7075-T6 and safety factor of 3 as discussed before). The ANSYS-optimized part was then imported into the CAD model. Figures 2.20 and 2.21 show the progression of some intermediate support frame designs; Figure 2.22 shows the final support frame CAD model with stress distributions.

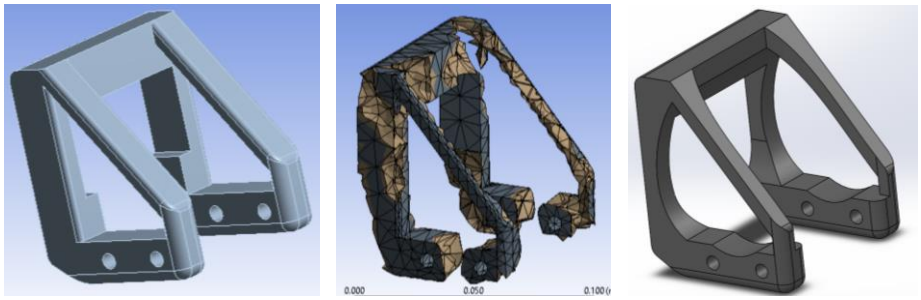

(a) (b) (c)

**Figure 2.20** Progression of support frame from (a) original design to (b) raw topologically optimized design to (c) finished optimized part.

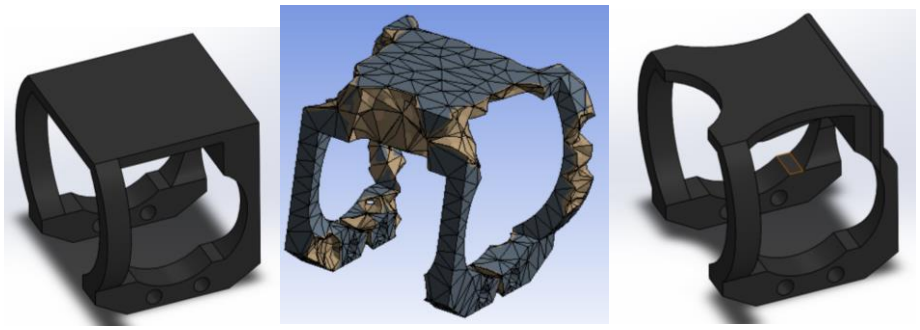

(a) (b) (c)

**Figure 2.21** Progression of an early support frame design with (a) original design (b) Raw topologically optimized part (c) Finished optimized part

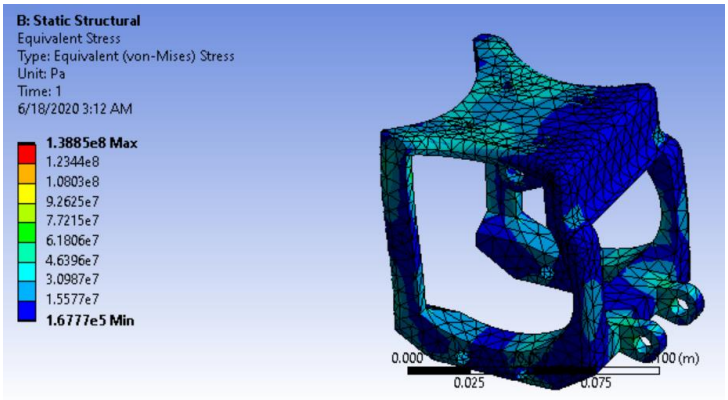


**Figure 2.22** Simulated von Mises stress distributions for the peak torque condition at $\theta$ =0.15 rad based on the biomechanical data from an able-bodied 75 kg able-bodied individual (Gates, 2004) of the final support frame

As can be seen from the stress distributions for all the parts, the peak stress in the support frame (138.85 MPa) was well within the required 167.67 MPa and the peak stresses in the support clevis and crank were 22.875, and 62.17 MPa and were thereby well within the desired value of 145 MPa. While this suggests that the parts are structurally overdesigned, it must be noted that the manufacturability of the parts was a more significant driving factor in the part design than mass optimization. Figure 2.23 shows the final manufactured prototype.

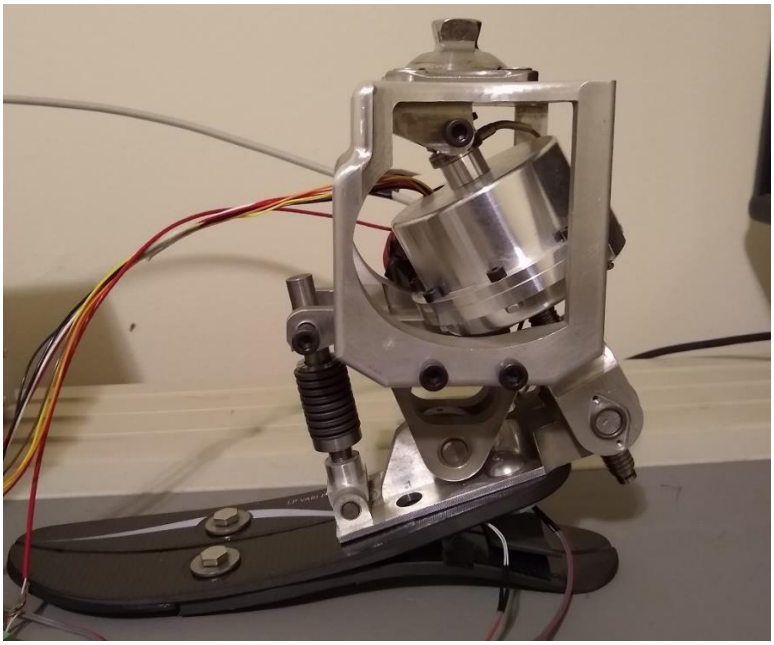

**Figure 2.23** The fabricated prototype

## 2.4 Control strategy and implementation

During human locomotion, the human ankle is known to continuously modulate its stiffness (slope of the torque-angle curve), also known as ankle impedance; this modulation occurs reflexively or voluntarily to accommodate stable locomotion, postural stabilization, propulsion, and smooth transition from stance to swing and vice versa (Lee, and Hogan, 2015; Rouse, *et al.*,

2014). This makes an impedance-based strategy appropriate for controlling the ankle prosthesis. This mapping of ankle torque to ankle position enables the user-prosthesis interaction to achieve a normal gait, within the limits of device dynamics.

Impedance control is typically implemented as a Proportional+Derivative (PD) control law as given in Equation (15), where $K$, $B$, $\theta_e$, $\theta_{ankle}$ and $\tau_{ankleref}$ represent the parameters for stiffness, damping, equilibrium angle[3], ankle angle, and desired (reference) ankle torque for a gait cycle phase, respectively.

$$\tau_{ankleref} = K(\theta_e - \theta_{ankle}) + B(\dot{\theta}_e - \dot{\theta}_{ankle}) \quad (15)$$

The practical implementation of this impedance control law requires compensation of the inherent mechanical friction and inertial dynamics of the device. This can be achieved via inner loop torque compensation (Ott, *et al.*, 2004; Ott, *et al.*, 2006). Consider the simplified rotor of Figure 2.24, subject to an external mechanical load torque ($\tau_{load}$), and applied motor torque ($\tau_{motor} = k_t\, i_m$) with inherent rotor parameters of damping ($b$), rotor inertia ($I_{rotor}$), and motor angle ($\gamma$).

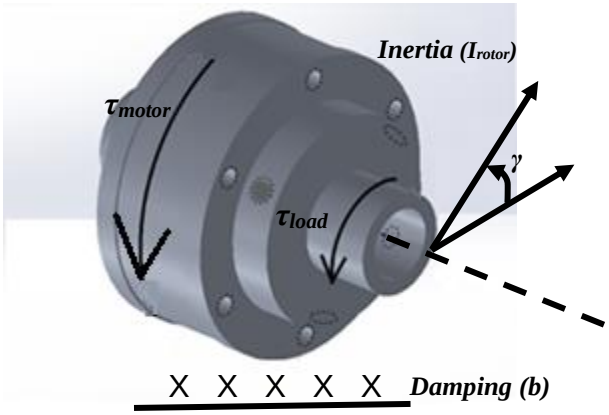


**Figure 2.24** Simplified rotor representation. $\tau_{motor}$, $\tau_{load}$, $b$, $I_{rotor}$, *and* $\gamma$ represent the actual motor torque, the translated or external load torque (from the contact force along the ball screw), the equivalent system damping at the rotor, the equivalent system inertia at the rotor, and the rotor angle respectively.

[3] This is the angle of the virtual spring of the controller and has no connection with the spring equilibrium angle

The applied motor torque can be expressed

$$\tau_{load} + \tau_{motor} = I_{rotor}\ddot{\gamma} + b\,\dot{\gamma} \tag{16}$$

The load torque $\tau_{load}$ can be substituted into the equation (17) for desired torque $\tau_d$ providing equation (18)

$$\tau_{motor} = \tau_d + k_f\,(\tau_{load} + \tau_{motor}) \tag{17}$$

$$I_{rotor}\,(1 - k_f)\,\ddot{\gamma} + b(1 - k_f)\,\dot{\gamma} = \tau_{load} + \tau_d \tag{18}$$

Hence, by using load torque feedback, internal mechanical impedance (due to friction and inertia) can be compensated.

The real-time control system was implemented using the TwinCAT3–Simulink RT interface on a Windows 7 OS Desktop, providing a user-friendly control interface wherein model implementations and changes can be easily performed. This interface used the EtherCAT (Ethernet for Control and Automation Technology) protocol, which has benefits over standard Fieldbus systems (CAN, Profibus, SERCOS, etc.) of reduced jitter (variation in the signal time from its nominal value), more precise clock synchronization, and higher bus cycle bandwidth, which enables cycle times in the microsecond range (Langlois, *et al.*, 2018). The extensive research and development of Ethernet have made the relevant hardware cheap and readily available. For this study, the TwinCAT 3-Simulink RT-based controller was operated at a sampling rate of 1 kHz. A schematic of information flow and connections is shown in Figure 2.25.

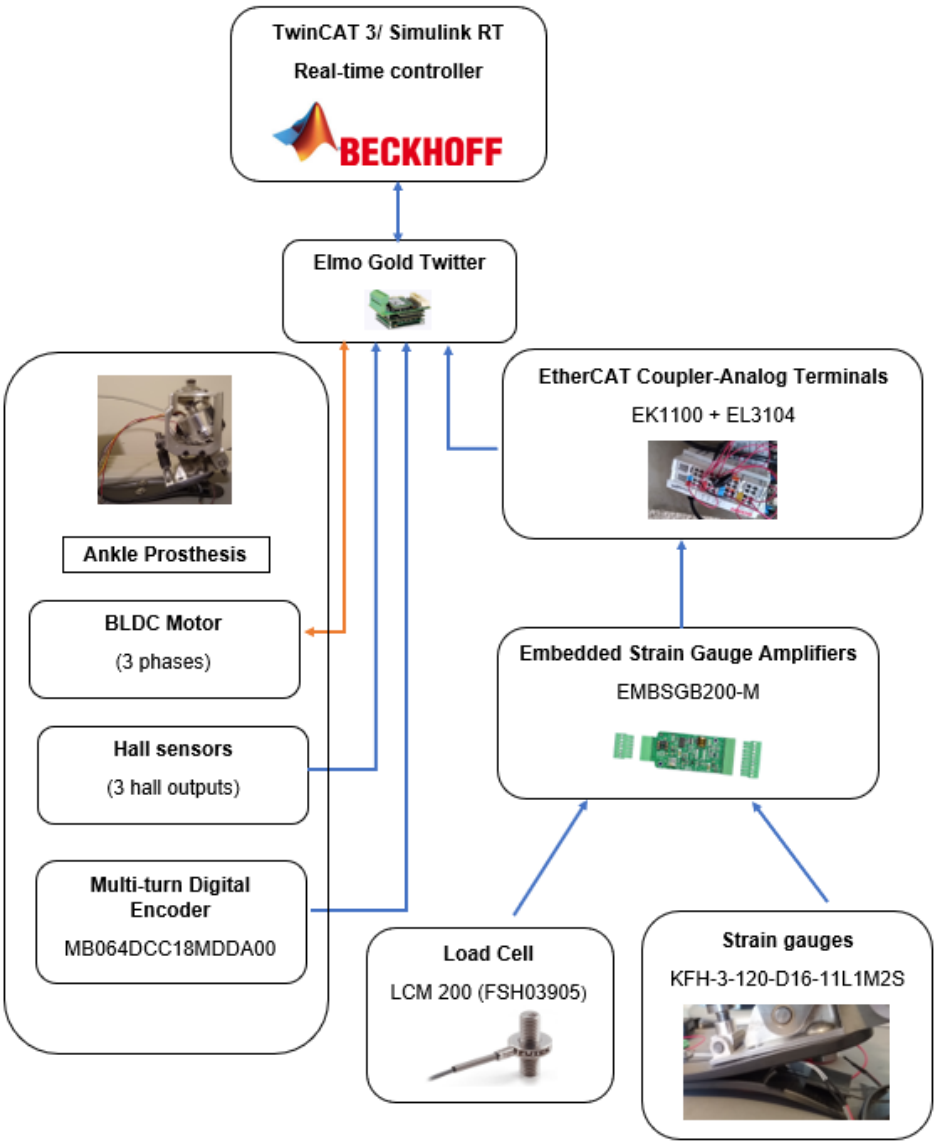


**Figure. 2.25** Electrical and data flow chart for the ankle prosthesis. Power lines (orange) and data lines (blue) are shown.

The BLDC motor was controlled using an Elmo Gold Solo Twitter servo drive (Elmo Motion Control model G-SOLTWIR50/100EE1S) via the current control mode. This motor has an embedded 18-bit multi-turn absolute BISS-C digital encoder (RLS model MB064DCC18MDDA00) which, along with the stator-embedded Hall effect sensors, is connected to the servo drive. The motor encoder is used to compute the ankle angle using the kinematic

equations derived in Section 2.2. A strain gauge load cell (FUTEK model FSH03905) was implemented in-line with the actuator. Two pre-wired strain gauges (OMEGA model KFH-3-120-D16-11L1M2S) are mounted between the heel section and crank mount sections of the prosthetic foot in a half-bridge resistive circuit. The load cell uses an amplifier from Tacuna Systems (model EMBSGB200-M), the output of which is connected to the Beckhoff differential four input analog terminal (model EL3104). This terminal is connected via a Beckhoff EtherCAT coupler (model EK1100) to the servo drive using an RJ45 Ethernet Cable. Finally, the servo drive is connected to the desktop computer using an RJ45 Ethernet Cable. The EtherCAT coupler and Elmo Gold Twitter are powered by a 24 V, 40 A power source (Mean Well model RSP-1000-24), while the load cell amplifiers are powered using standard 9V PP3 batteries.

The control diagram is shown in Figure 2.26. The impedance controller is implemented as a PD controller with fixed reference angle (or equilibrium angle $\theta_e$), stiffness (or proportional gain $K$), and damping (or derivative gain $B$) values (individual gait phases can be well characterized by such fixed parameters derived from the torque angle curves). The input of the impedance controller is the ankle angle $\theta$ and the output is the desired ankle torque $\tau_{ankleref}$. The desired ankle torque is then processed using transmission ration $T_r(\theta)$ to obtain the reference motor torque $\tau_{motorref}$. Here, the load cell $F$ and motor current $i_m$ feedback values are then used to compute the feedback compensation $\tau_{load}$, which is then added to the reference motor torque. The reference motor torque is then used to compute the reference current $i_{mref}$. The servo drive then provides the BLDC motor's current $i_m$. This generates the required torque output at the ankle $\tau_{ankle}$.

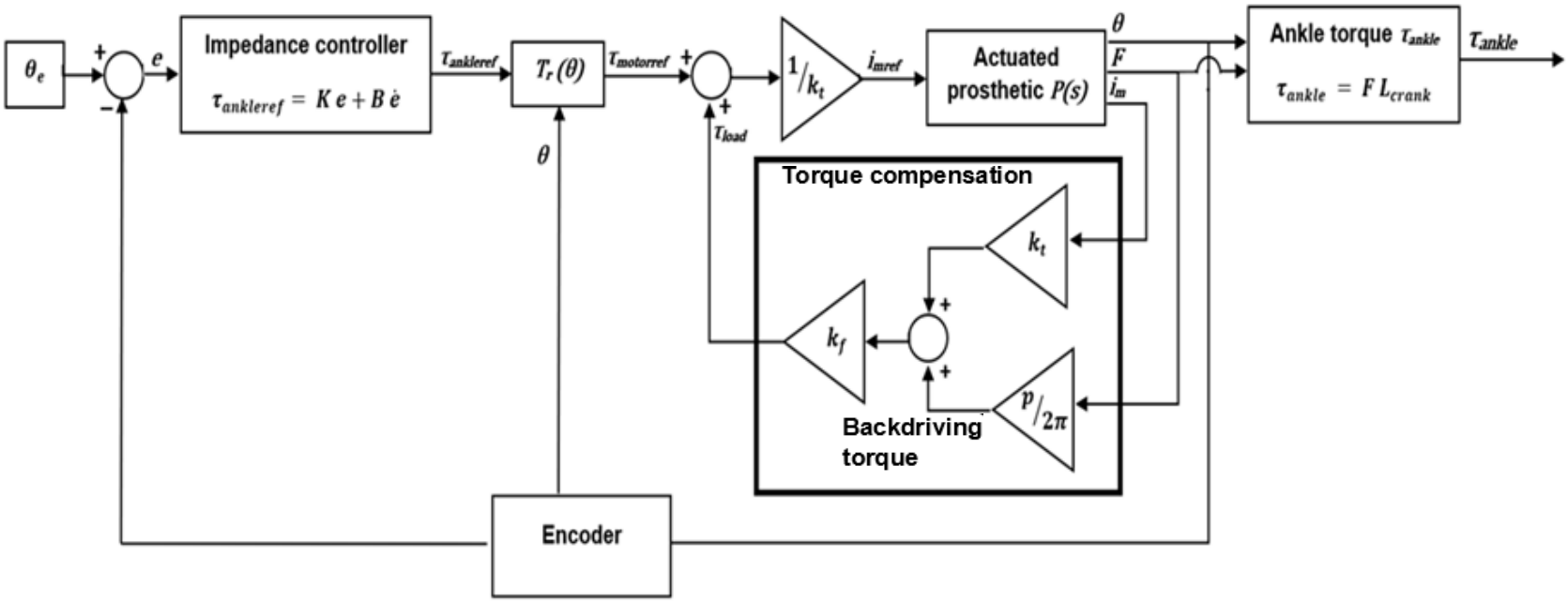


**Figure 2.26** Proposed control diagram for the system

## 2.5 Setup for validation of ankle prosthesis

For testing, the ankle device was mounted on an Instron 4400R universal testing machine as shown in Figure 2.27 and 2.28. The prosthetic foot was removed due to space considerations and the required parts were machined for mounting on the UTM. The setup forms a 4-bar linkage with the ankle point (fixed to the lower jaw) acting as a slider (vertically) while the upper jaw and crank act as two pivoted movable links. The lower jaw (slider) provides a triangle wave position input. The setup is discussed in further detail in the following paragraphs.

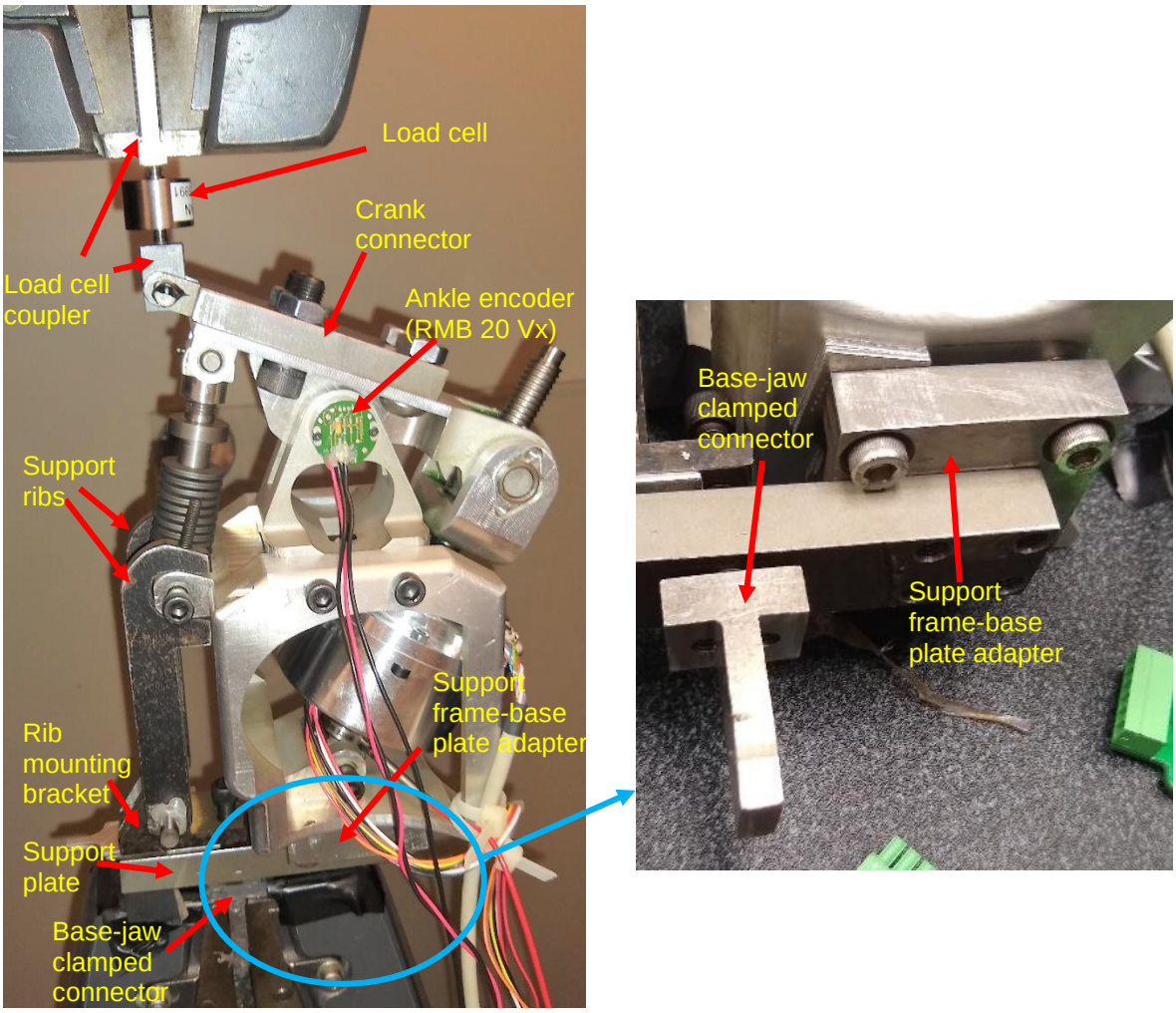


**Figure 2.27** Ankle device testing on the Instron 4400R UTM. All parts highlighted above are applicable only for the test setup. The real-time use of the prosthesis will have the structure as shown in Section 2.3

An ankle angle sensor (Renishaw RLS model RMB20Vx) and motor encoder (Renishaw RLS model MB064DCC18MDDA00) were used to measure ankle angles for the passive element and actuator, respectively. The crank was fastened to the crank connector using four 3/8-24 bolt-nut assemblies. The crank connector was then connected to an l kN capacity inline load cell (LCM systems model DCE-1KN) via a custom coupler (forming a revolute joint with the crank connector). Another custom threaded coupler was secured to one end of the load cell and clamped in the UTM's upper jaw. Two customized support ribs were mounted on the support frame of the prosthesis to provide moment rigidity. The ribs were further mounted on the rib mounting bracket (via a pinned revolute joint). This bracket was then bolted to the support base plate. For mounting the prosthesis, the pyramid adapter of the prosthetic foot was removed, and a customized adapter connected the support plate and support frame (shown in Figure 2.27). The support base plate was bolted to the base-jaw clamp connector (clamped in the lower jaw). Figure 2.28 provides a view of the complete setup (the data acquisition is as described in Section 2.4).

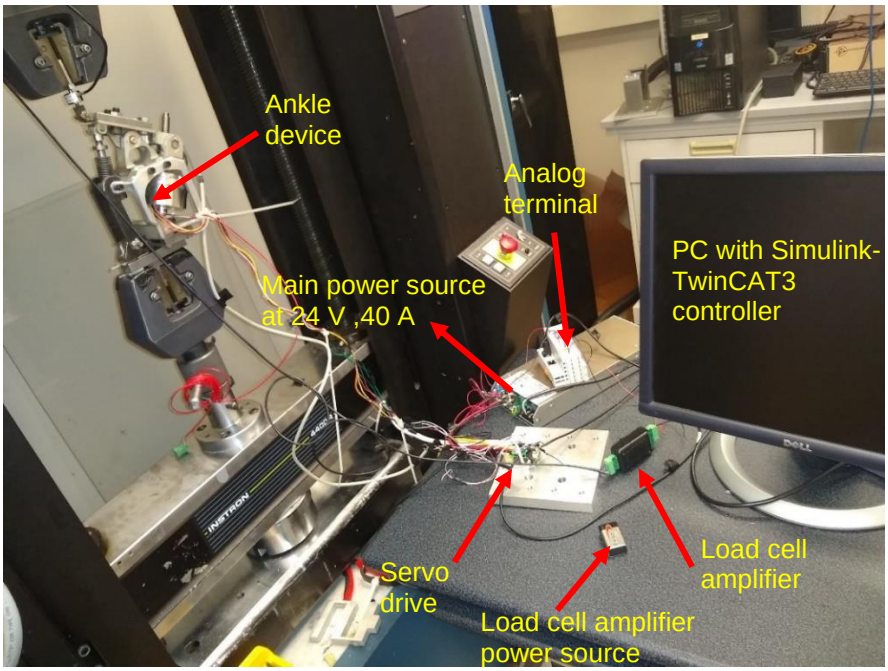


**Figure 2.28** Ankle testing with the electronic setup shown

# CHAPTER 3. RESULTS

## 3.1 Motion bandwidth

An important requirement for the ankle device is the ability to track the required ankle angles with sufficient bandwidth. A human gait frequency analysis shows that the highest frequency bandwidth lies in the range of 1-2 Hz (Satkunskiene, *et al.*, 2009). To accomplish this, a PD controller was tuned in the servo drive's velocity control mode for a 5° step response (shown in Figure 3.1) to achieve the required response.

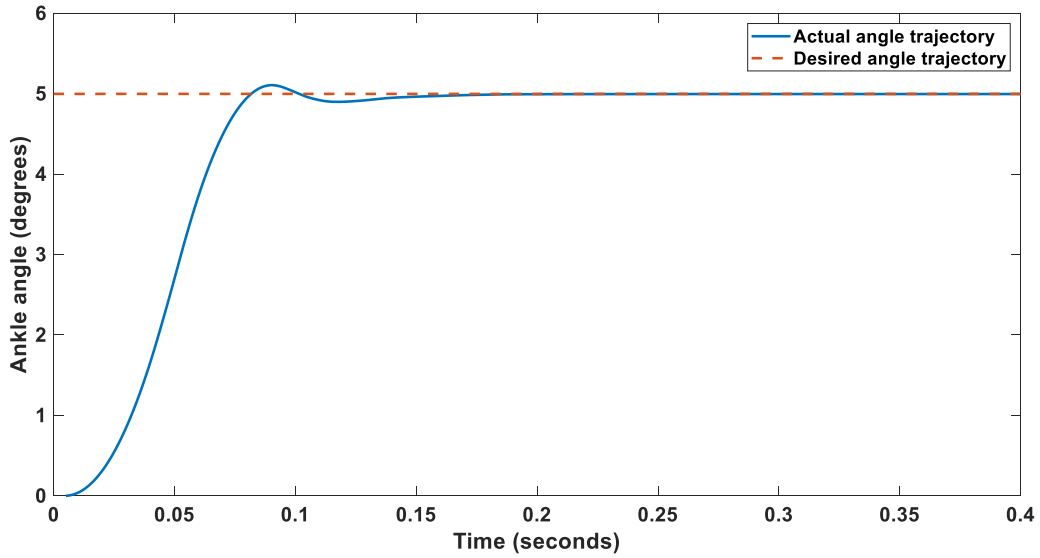


**Figure.3.1** Comparison of reference and actual ankle angle trajectories for a 5° step response

Figure 3.1 reveals a rise time of 0.07 seconds, a settling time of 0.079 seconds, and an overshoot of 2%. The bandwidth assessment was conducted for angle tracking of 5° and 10° at 2.0 and 1.8 Hz, respectively (shown in Figure 3.2).

Figure 3.2 (a) and (b) show the device's response to sinusoidal references of 5° and 10° at 2.0 Hz and 1.8 Hz (due to power source limitations), respectively. The peak and RMS tracking

errors (arising from a phase shift and a slight output magnitude reduction of 3.2% and 2.4% for 5° and 10° respectively) were 1.52° and 1.07° for 5° at 2 Hz and 2.70° and 1.91° for 10° at 1.8 Hz.

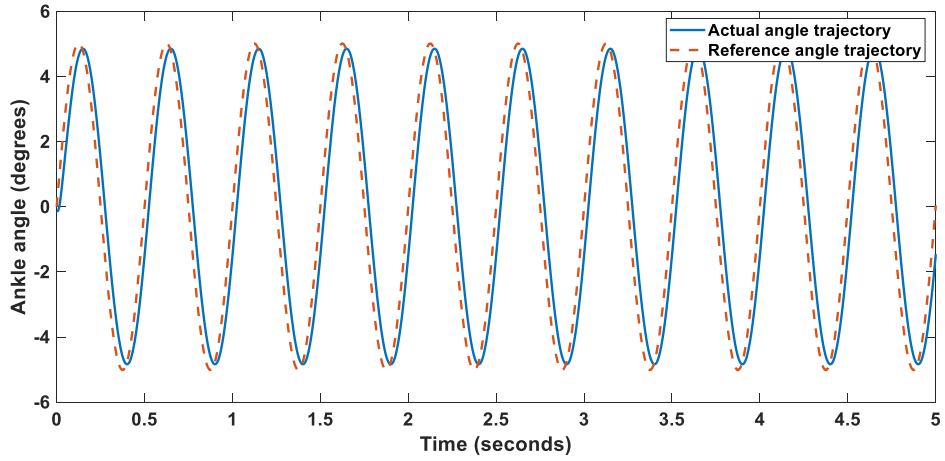


(a)

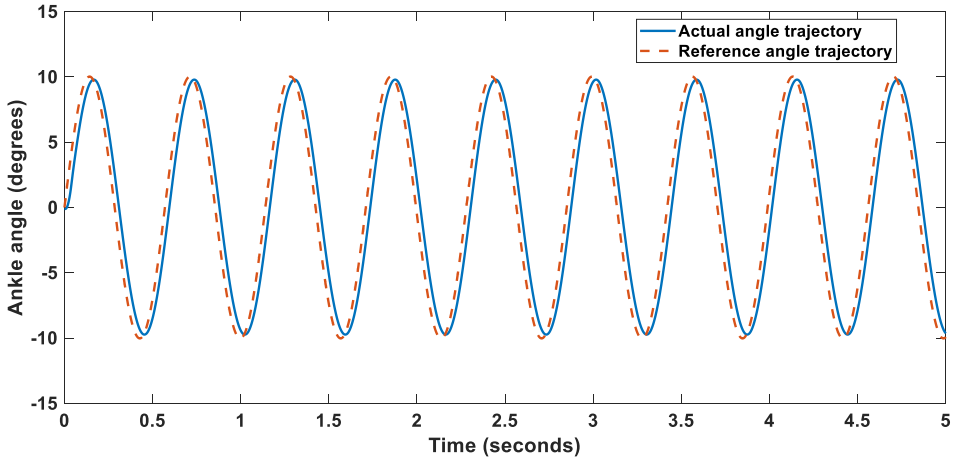


(b)

**Figure.3.2** Comparison of reference and actual ankle angle trajectories for **(a)** 5° at 2 Hz **(b)** 10° at 1.8 Hz

## 3.2 Passive element characteristics

Experiments were conducted to study the stiffness and equilibrium angle characteristics of the passive element. For this, different stack configurations providing gait-tuned angular stiffness

($k_{spring}$) and equilibrium angle ($\theta_o$) values were used. The individual configurations were $k_{spring}$ = 227.57 Nm/rad at $\theta_o$ = 0.10 rad for stair ascent, $k_{spring}$ = 342.59 Nm/rad at $\theta_o$ = -0.07 rad for walking, and $k_{spring}$ = 403.33 Nm/rad at $\theta_o$ = 0.00 rad for the current configuration. The actuator was removed for this test. The testing was conducted by providing a triangle wave position input using the UTM jaws and measuring the ankle angle sensor output and load cell output (and thereby the ankle torque). The torque-angle curves are shown in Figure 3.3.

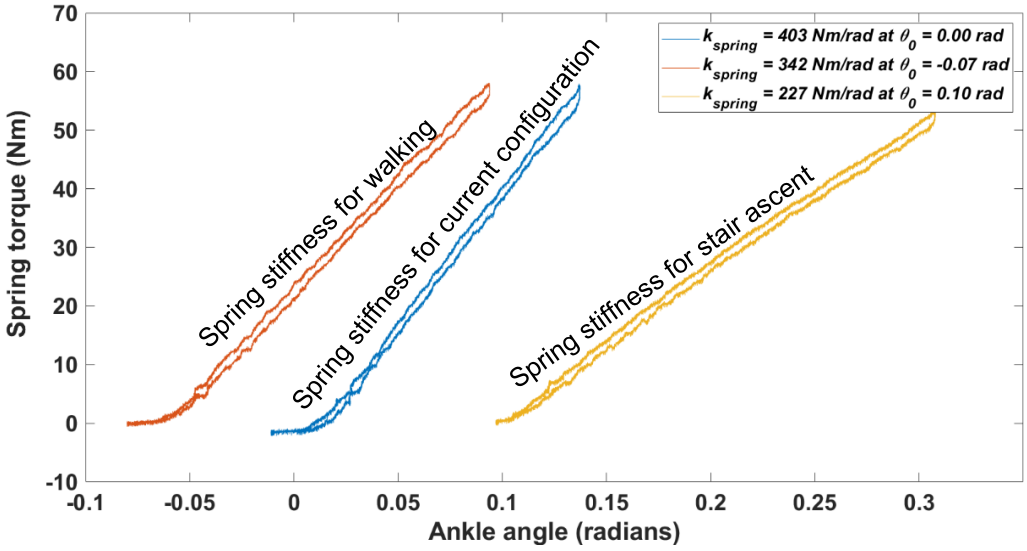


**Figure 3.3** Spring torque-ankle angle curves for different configurations of angular stiffness $k_{spring}$ and equilibrium angle $\theta_o$.

Figure 3.3 reveals absolute mean torque error-to-peak torque and peak torque error-to-peak torque (from mean average line for individual spring configurations) percentage ratios of 1.55 % and 3.52 % for the current configuration, 1.79 % and 4.12 % for walking, 1.55 % and 4.95 % for stair ascent.

### 3.3 Backdrivability assessment and mechanical impedance compensation

This experiment desires to quantify the device backdrivability with and without torque feedback. For this, an external manual torque was applied to the device and the ankle torque and angle data were collected. Figure 3.4 shows the variation in backdriving torque for feedback gain $k_f$ = 0.00 (no feedback condition) and $k_f$ = 0.75. The resulting peak back driving torques were 7.61 Nm for $k_f$ = 0.00 and 2.04 Nm for $k_f$ = 0.75, respectively. confirming the desired ankle backdrivability.

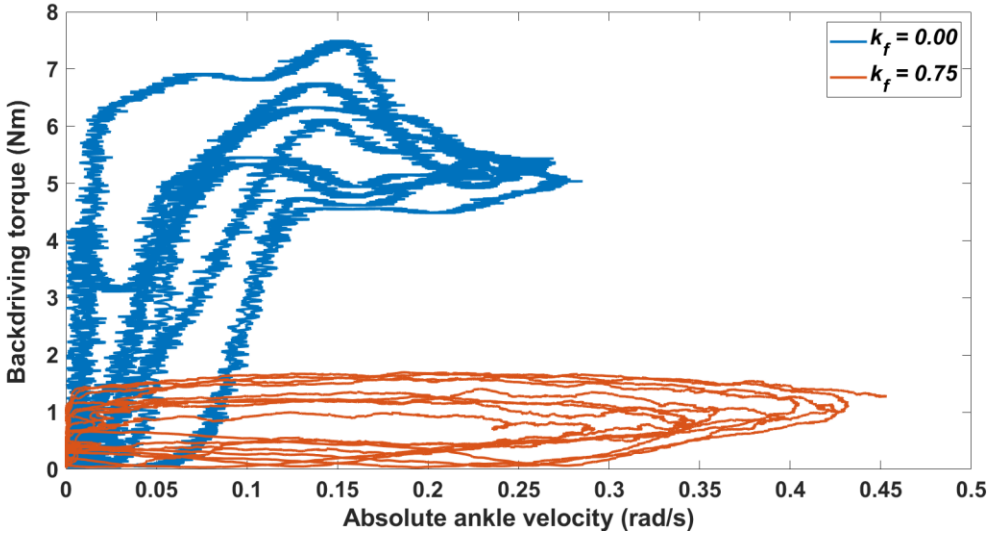


**Figure 3.4** Variation in back driving torques with feedback gain $k_f$. The figure reveals the inherent device back drivability (back driving torque in the manually achievable range of 4.5-7.6 Nm) and an increase in device back drivability with an increase in feedback gain. The loops formed were caused by the system inertia.

### 3.4 Torque tracking characteristics

To validate the torque tracking characteristics of the device, the jaws of the UTM were clamped. Then, the Simulink model (controller) implemented a sinusoidal torque output of amplitude 21.5 Nm, from 4.3 Nm (to maintain a preload for backlash mitigation) to rated torque 47.3 Nm. The feedback gain was set to $k_f$ = 0.75 and frequencies from 0.17 to 0.67 Hz were studied

(the assessment was stopped at 0.67 Hz due to potentially harmful vibrations). Figure 3.5 shows the torque trajectories, thus obtained, for 0.5 Hz and 0.67 Hz, respectively.

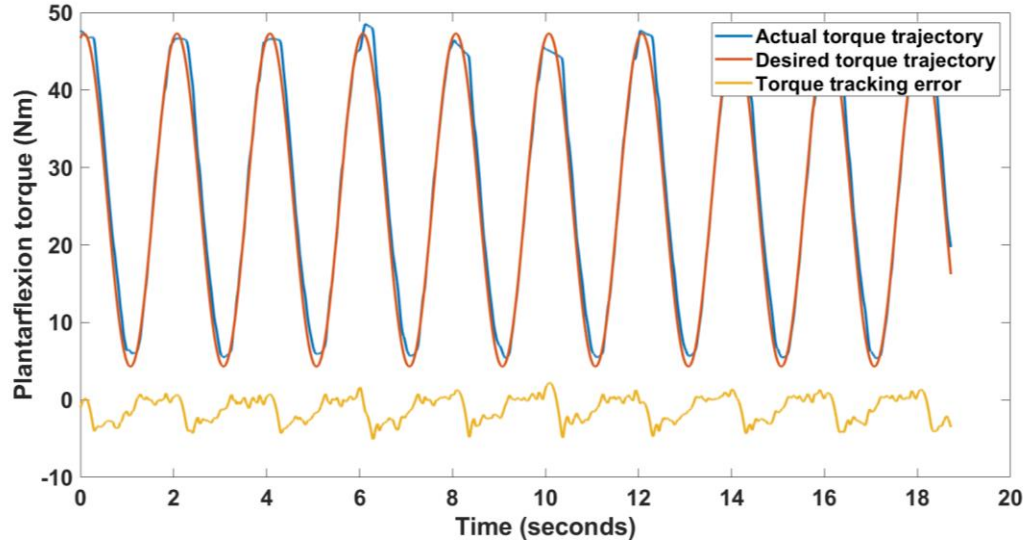


(a)

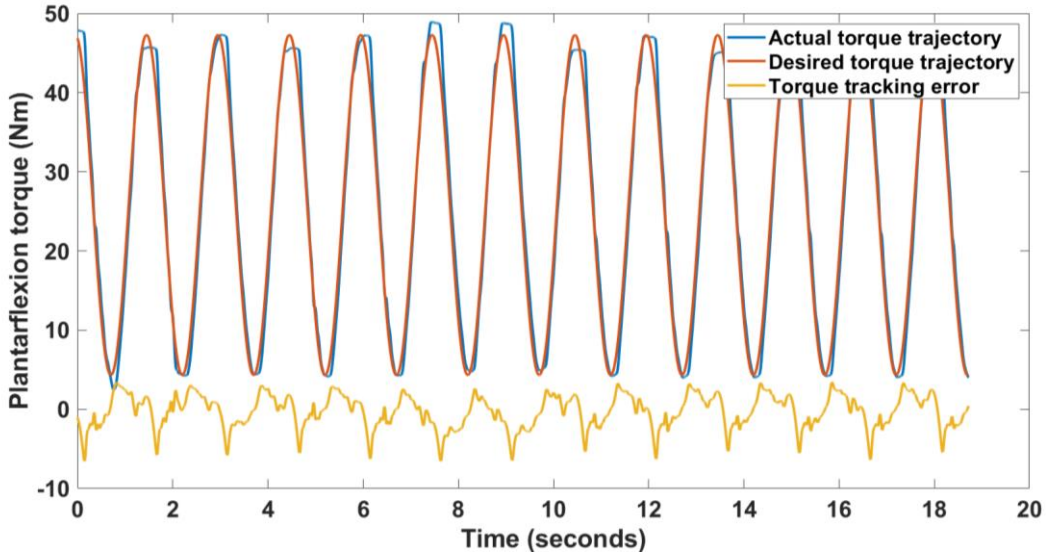


(b)

**Figure 3.5** Comparative chart of actual and desired torque tracking at **(a)** 0.5 Hz **(b)** 0.67 Hz.

The torque tracking curves reveal mean and peak error values of 1.50 Nm and 5.09 Nm at 0.5 Hz and 3.30 Nm, respectively, and 9.53 Nm for 0.67 Hz. Figure 3.6 shows the frequency

response curves of mean and peak amplitudes for frequencies from 0.17 to 0.67 Hz. The amplitude increase from 0.33 Hz to 0.67 Hz indicates a dependency of friction on the torque loading rate.

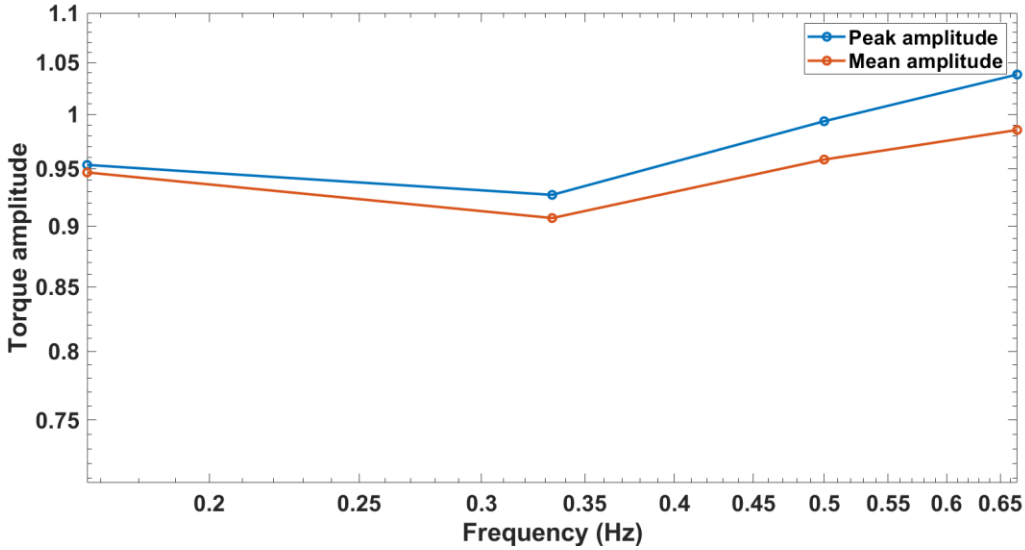


**Figure 3.6** Frequency response curves for peak and mean torque amplitudes

### 3.5 Impedance control tests

For impedance control demonstrations, two biomechanically relevant impedance values were selected (based on the able-bodied torque-angle curves and current spring stiffness, as discussed in Section 2.2). The parameters were $k_{PP}$ = 162.4 Nm/rad for ankle angles from -0.30 to -0.03 (derived from powered plantarflexion) and $k_{CD}$ = 179.2 Nm/rad for ankle angles from -0.125 to 0.00 (derived from controlled dorsiflexion). The feedback gain $k_f$ was set to 0.67. The UTM jaws provided the triangle wave position input to induce the necessary external input. Figure 3.7 shows the torque tracking for the impedance control parameters. A high frequency (approximately 10 Hz) undesirable oscillatory signal was found in the output, potentially due to higher-order dynamics (stick-slip) and system vibrations. Hence, the load output was post-processed using a moving mean filter with a window size of 200 samples and a sampling of rate 1.0 kHz (raw output

is shown in Appendix C). The mean and peak error values were found to be 2.48 Nm and 6.20 Nm for $k_{PP}$ = 162.4 Nm/rad and 1.63 Nm, respectively, and 3.91 Nm for $k_{CD}$ = 179.2 Nm/rad.

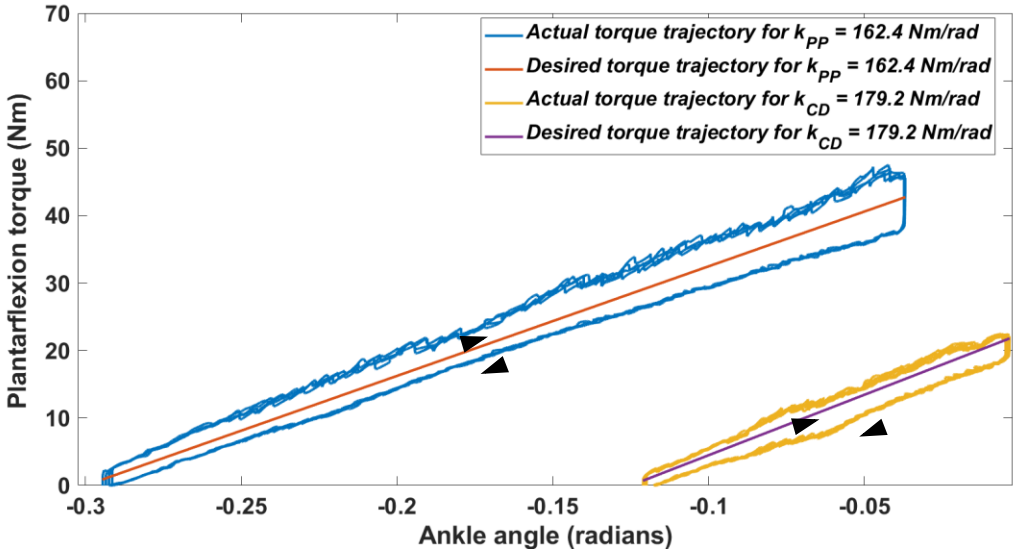


**Figure 3.7** Impedance control tests for $k_{PP}$ = 162.4 Nm/rad (derived from powered plantarflexion for current spring configuration) and $k_{CD}$ = 179.2 Nm/rad (derived from controlled dorsiflexion for current spring configuration) for a feedback gain $k_f$ = 0.67 (arrowheads indicate the direction of motion). The sudden discontinuities at the curve peaks can be attributed to change in the direction of stiction with a reversal in motion direction.

Figure 3.8 (a) and (b) show the current characteristics for the aforementioned powered plantarflexion and controlled dorsiflexion curves (derived for current spring configuration). The feedback currents show asymmetric behavior for loading and unloading for both $k_{PP}$ = 162.4 Nm/rad and $k_{CD}$ = 179.2 Nm/rad, indicating frictional anisotropy. Figure 3.9 shows the error characteristics for these curves from the desired torque trajectories; it reveals that the ratio of torque tracking error to desired torque shows absolute initial values of 1.39 for $k_{PP}$ = 162.4 Nm/rad and 1.53 for $k_{CD}$ = 179.2 Nm/rad. The ratios approach near-constant values of 0.11 for $k_{PP}$ = 162.4 Nm/rad and 0.12 for $k_{CD}$ = 179.2 Nm/rad, as peak torques are achieved. This behavior indicates the dependency of friction on load.

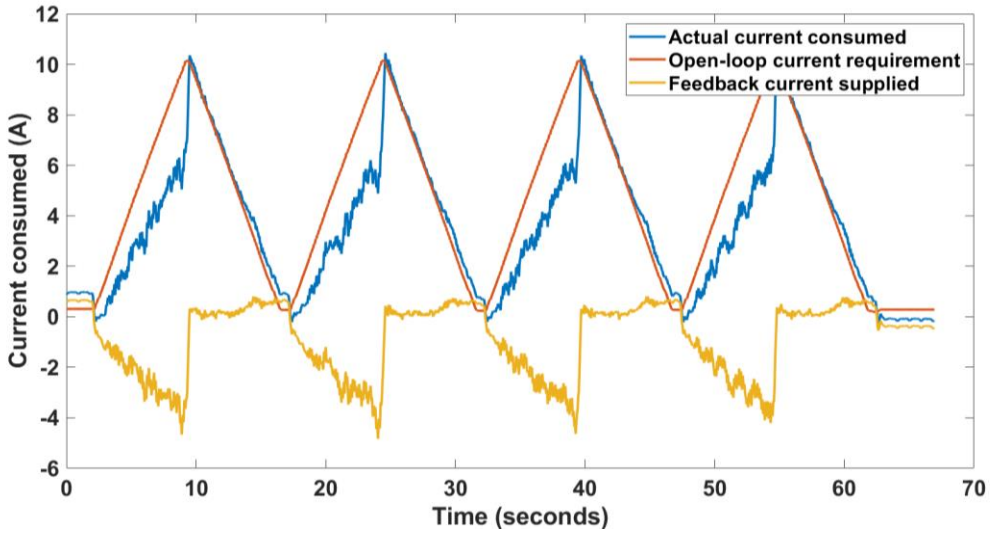


(a)

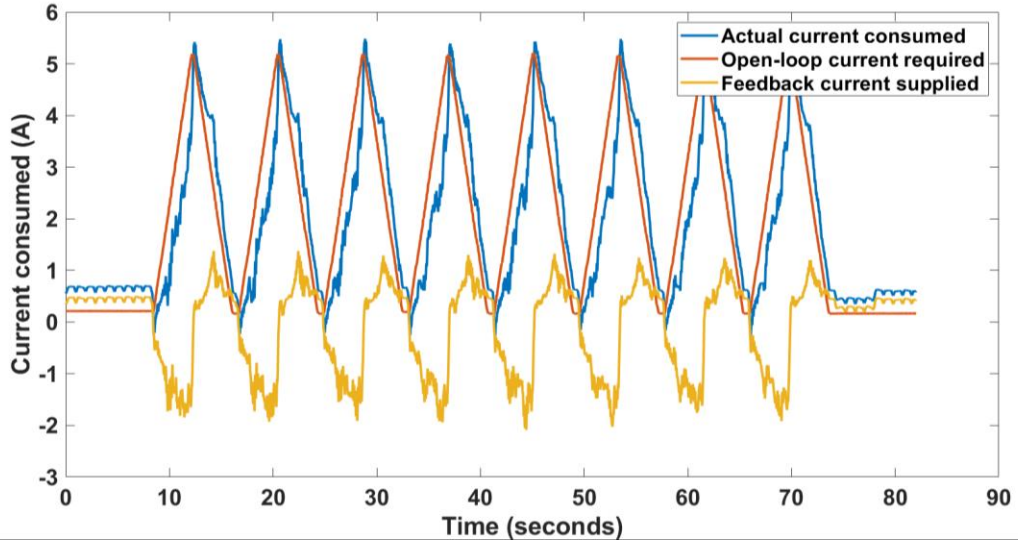


(b)

**Figure 3.8 (a)** Current characteristics for $k_{PP}$ = 162.4 Nm/rad (derived from powered plantarflexion for current spring configuration) **(b)** Current characteristics for $k_{CD}$ = 179.2 Nm/rad (derived from controlled dorsiflexion for current spring configuration)

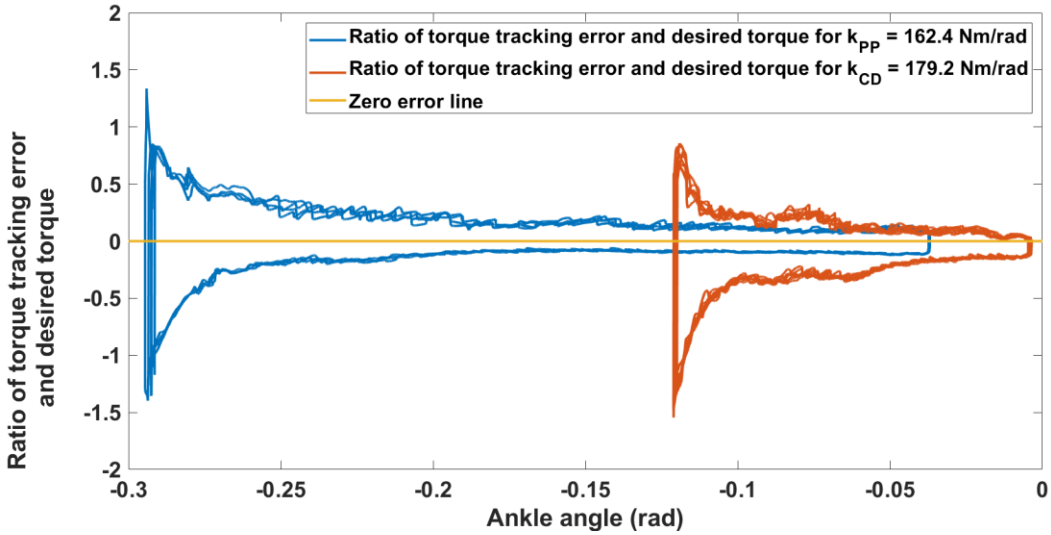


**Figure 3.9** Torque tracking error characteristics for $k_{PP}$ = 162.4 Nm/rad (derived from powered plantarflexion for current spring configuration) and $k_{CD}$ = 179.2 Nm/rad (derived from controlled dorsiflexion for current spring configuration)

# CHAPTER 4. DISCUSSION AND FUTURE SCOPE

The *VSeM Ankle* prosthesis, detailed in this document, demonstrated promising performance and satisfied the design objectives outlined in the Introduction (Section 1) with respect to device weight (1.9 kg without electronics), height (22 cm with foot cover), and range of motion (55º, 0.96 rad). The passive element provides the required range in parallel spring stiffness and equilibrium angle along with low hysteresis (1.5% mean error-to-peak torque ratio), as revealed by Figure 3.4. Furthermore, the device exhibits a 5º step response settling time of 79 milliseconds and desirable motion bandwidth (amplitude reductions of only 3.2% at 5º, 2 Hz and 2.4% at 10º, 1.8 Hz), which exceed the design requirements. The device exhibits backdriving torques in the manually achievable range of 4.5-7.6 Nm. Moreover, clamped bandwidth testing at rated torque (47.3 Nm) showed a bandwidth greater than 0.5 Hz while indicating an increasing trend in the amplitude beyond 0.67 Hz. Then, the impedance control shows low hysteresis (5.9% mean error-to-peak torque ratio for $k_{PP}$ = 162.4 Nm/rad) while achieving the peak torque requirements of the device. Table 4.1 compares the *VSeM Ankle* with other state-of-the-art powered ankle prostheses (only ankle prostheses i.e. prostheses which are designed as combined knee-ankle prostheses not shown). Table 4.1 reveals the improved range of motion, due to passive element adaptability, of the *VSeM Ankle* over most other devices. This characteristic, coupled with the highest dorsiflexion range of motion, improves the utility of the *VSeM Ankle* for gaits such as the sit-to-stand transitions when compared to other devices. Additionally, the *VSeM Ankle* shows comparable specifications for mass, height, and peak torque with the other prostheses shown. All the devices compared use variations of the four-bar linkage mechanism.

**Table 4.1** Comparison of the VSeM Ankle with other prosthetic ankles (Gabert, *et al.*, 2020; Grimmer, *et al.*, 2016; Shultz, *et al.*, 2016).

| ***Device*** | ***Actuation mechanism*** | ***Passive element*** | ***Range of motion (°)*** | ***Mass (kg)*** | ***Build height (cm)*** | ***Peak torque (Nm)*** |
|---|---|---|---|---|---|---|
| VSeM (NCSU)  | Motor + Ball screw | Variable stiffness and equilibrium angle spring (parallel) | +30 / – 25 | 1.9* | 21 | 140 |
| BIOM (MIT)  | Motor + Timing belt + Ball screw | Fixed leaf springs (series and parallel) | +10 / – 24 | 2.2 | 19 | 125 |
| OSL (UMich)  | Motor + Timing belt | None | 30 | 1.74 | 21.3 | 140 |
| VU Leg 3 (Vanderbilt)  | Motor + Timing belt | Fixed carbon fiber leaf spring (parallel) | +20 / – 45 | 2.3 | 21 | 140 |
| Walk-Run (SpringActive)  | Motor + Timing belt + Roller screw | Fixed coil spring (series) | +10 / – 30 | 1.9* | 30 | 140 |
| UMass Ankle (UMass)  | Motor + Timing belt + Ball screw | None | +0 / – 10 | 1.9* | 18.4 | 100 |
| *excluding electronics and battery | | | | | | |

Interesting device characteristics and limitations were revealed during testing, most notably in the actuator. Motion tracking revealed a power supply shut off for $10^{\circ}$ at 2 Hz. This limited the motion tracking frequency for $10^{\circ}$ to 1.8 Hz. This indicates a need to include power source compatibility as a consideration at the actuator design stage.

The device's frictional characteristics, as revealed in Sections 3.3-3.5, deserve special attention. Despite being backdrivable, the device's mechanical impedance was not low enough to facilitate the use of open-loop torque control. Hence, the use of a load cell/torque sensor becomes unavoidable. Furthermore, the impedance control tests showed significant deviations from the desired torques at lower torques (up to 53 %), as revealed in Figure 3.10. This behavior can be attributed to stiction. Additionally, an undesirable oscillatory signal (approximately 10 Hz) was observed in the load cell output during impedance control tests. This may have been caused by potential damage to the ball nut/screw or angular contact bearings. This issue may be readily resolved via replacement with new parts. However, the inherent frictional dynamics tend to be highly nonlinear and multifactorial (dependency on load, loading rate, velocity, motion direction, motor angle, lubrication status). Furthermore, while the force feedback does reduce the effects of friction, gain increments beyond $k_f = 0.8$ yield an unstable behavior. Hence, further reduction in frictional effects will need the development of an adaptive nonlinear friction model. Alternatively, a part design change (at connector-ball nut interface) incorporating a series elastic element may give the device improved friction characteristics.

Finally, the passive element torque-ankle angle readings reveal nonlinearity in the initial spring loading phase and low but unmodelled hysteresis. Hence, a new model for the passive element which incorporates the above two points will better indicate the exact properties of the passive element.

This work attempts to answer some research questions in the community but the scope for further exploration is quite vast. The future work around this device will involve the exploration of advanced prosthesis control. Current studies do not show a clear advantage of active ankle prosthesis over energetically passive devices (Fylstra, *et al.*, 2020; Gardinier, *et al.*, 2018), potentially due to prosthesis control incoordination. Designing optimal, adaptive control of active prosthesis (Huang, He, *et al.*, 2016; Wen, *et al.*, 2020) and developing human training tools (Brandt,& Huang, 2019) (Huang, H., *et al.*, 2009)an be crucial to address human-prosthesis coordination. Another potential solution is to explore neural control of this active prosthesis (Fleming,& Huang, 2019; Huang, *et al.*, 2009). All these studies will be extensions of this design whose goal is to improve the quality of life for individuals with lower-limb amputations.

Furthermore, future device development may be conducted with the design of a device with low impedance. Such a device may utilize the existing spring element design or utilize a high torque actuator with an extremely efficient cooling system. Finally, the existing passive element is largely limited to research purposes due to offline control of the equilibrium angle. For commercial implementation, online control of the equilibrium angle may be quite useful.

## REFERENCES

3M. (2019). *3M scotch-weld epoxy adhesive* 3M.

AB SKF. (2013). *Precision rolled ball screws*

Adamczyk, P. G. (2020). Ankle control in walking and running: Speed- and gait-related changes in dynamic mean ankle moment arm. *Journal of Biomechanical Engineering, 142*(7) doi:10.1115/1.4045817

Aguirre-Ollinger, G., Colgate, J. E., Peshkin, M. A., & Goswami, A. (2007). (2007). Active-impedance control of a lower-limb assistive exoskeleton. Paper presented at the 188-195. doi:10.1109/ICORR.2007.4428426

ASM Handbook Committee. (1990). *Properties and selection: Nonferrous alloys and special-purpose materials* ASM International. doi:10.31399/asm.hb.v02.9781627081627 Retrieved from https://doi.org/10.31399/asm.hb.v02.9781627081627

Au, S. K., Weber, J., & Herr, H. (2007). (2007). Biomechanical design of a powered ankle-foot prosthesis. Paper presented at the 298-303. doi:10.1109/ICORR.2007.4428441

Au, S., Berniker, M., & Herr, H. (2008). Powered ankle-foot prosthesis to assist level-ground and stair-descent gaits. *Neural Networks; Robotics and Neuroscience, 21*(4), 654-666. doi:https://doi.org/10.1016/j.neunet.2008.03.006

Azocar, A. F., Mooney, L. M., Hargrove, L. J., & Rouse, E. J. (2018). (2018). Design and characterization of an open-source robotic leg prosthesis. Paper presented at the 111-118. doi:10.1109/BIOROB.2018.8488057

Bellman, R. D., Holgate, M. A., & Sugar, T. G. (2008). (2008). SPARKy 3: Design of an active robotic ankle prosthesis with two actuated degrees of freedom using regenerative kinetics. Paper presented at the 511-516. doi:10.1109/BIOROB.2008.4762887

Brandt, A., & Huang, H. (. H. (2019). Effects of extended stance time on a powered knee prosthesis and gait symmetry on the lateral control of balance during walking in individuals with unilateral amputation. *Journal of NeuroEngineering and Rehabilitation, 16*(1), 151. doi:10.1186/s12984-019-0625-6

Celera Motion.*Motor mounting guide* (REV 160701 ed.)

Celera Motion. (2018). *Product data sheet: Omni™ series motors* (REV190104 ed.) Celera Motion.

Elery, T., Rezazadeh, S., Nesler, C., Doan, J., Zhu, H., & Gregg, R. D. (2018). Design and benchtop validation of a powered knee-ankle prosthesis with high-torque, low-impedance actuators. *IEEE International Conference on Robotics and Automation : ICRA : [Proceedings].IEEE International Conference on Robotics and Automation, 2018*, 2788-2795. doi:10.1109/ICRA.2018.8461259

Fleming, A., & Huang, H. H. (2019). Proportional myoelectric control of a powered ankle prosthesis for postural control under expected perturbation: A pilot study. *IEEE ...International Conference on Rehabilitation Robotics : [Proceedings], 2019*, 899-904. doi:10.1109/ICORR.2019.8779509 [doi]

Fylstra, B. L., Lee, I., Huang, S., Brandt, A., Lewek, M. D., & Huang, H. (. (2020). Human-prosthesis coordination: A preliminary study exploring coordination with a powered ankle-foot prosthesis. *Clinical Biomechanics, 80* doi:10.1016/j.clinbiomech.2020.105171

Gabert, L., Hood, S., Tran, M., Cempini, M., & Lenzi, T. (2020). A compact, lightweight robotic ankle-foot prosthesis: Featuring a powered polycentric design. *IEEE Robotics & Automation Magazine, 27*(1), 87-102. doi:10.1109/MRA.2019.2955740

Gao, F., Liu, Y., & Liao, W. (2018). Design of powered ankle-foot prosthesis with nonlinear parallel spring mechanism. *Journal of Mechanical Design, 140*(5) doi:10.1115/1.4039385

Gardinier, E. S., Kelly, B. M., Wensman, J., & Gates, D. H. (2018). A controlled clinical trial of a clinically-tuned powered ankle prosthesis in people with transtibial amputation. *Clinical Rehabilitation, 32*(3), 319-329. doi:10.1177/0269215517723054 [doi]

Gates, D. H. (2004). No title. *Characterizing Ankle Function during Stair Ascent, Descent, and Level Walking for Ankle Prosthesis and Orthosis Design,*

Glanzer, E. M., & Adamczyk, P. G. (2018). Design and validation of a semi-active variable stiffness foot prosthesis. *IEEE Transactions on Neural Systems and Rehabilitation Engineering, 26*(12), 2351-2359. doi:10.1109/TNSRE.2018.2877962

Grimmer, M., Holgate, M., Holgate, R., Boehler, A., Ward, J., Hollander, K., . . . Seyfarth, A. (2016). A powered prosthetic ankle joint for walking and running. *Biomedical Engineering Online, 15*, 141. doi:10.1186/s12938-016-0286-7

Hagberg, K., & Brånemark, R. (2001). Consequences of non-vascular trans-femoral amputation: A survey of quality of life, prosthetic use and problems. *Prosthetics and Orthotics International, 25*(3), 186-194. doi:10.1080/03093640108726601 [doi]

Hitt, J. K., *et al.* (2007). *The SPARKy (spring ankle with regenerative kinetics) project: Design and analysis of a robotic transtibial prosthesis with regenerative kinetics; ASME 2007*

*international design engineering technical conferences and computers and information in engineering conference* doi:10.1115/DETC2007-34512

Hsu, M. J., Nielsen, D. H., Lin-Chan, S. J., & Shurr, D. (2006). The effects of prosthetic foot design on physiologic measurements, self-selected walking velocity, and physical activity in people with transtibial amputation. *Archives of Physical Medicine and Rehabilitation, 87*(1), 123-129. doi:S0003-9993(05)01136-6 [pii]

Huang, H., Kuiken, T. A., & Lipschutz, R. D. (2009). A strategy for identifying locomotion modes using surface electromyography. *IEEE Transactions on Bio-Medical Engineering, 56*(1), 65-73. doi:10.1109/TBME.2008.2003293 [doi]

Huang, H., Crouch, D. L., Liu, M., Sawicki, G. S., & Wang, D. (2016). A cyber expert system for auto-tuning powered prosthesis impedance control parameters. *Annals of Biomedical Engineering, 44*(5), 1613-1624. doi:10.1007/s10439-015-1464-7

Langlois, K., van der Hoeven, T., Rodriguez Cianca, D., Verstraten, T., Bacek, T., Convens, B., . . . Vanderborght, B. (2018). EtherCAT tutorial: An introduction for real-time hardware communication on windows [tutorial]. *IEEE Robotics & Automation Magazine, 25*(1), 22-122. doi:10.1109/MRA.2017.2787224

Lee, H., & Hogan, N. (2015). Time-varying ankle mechanical impedance during human locomotion. *IEEE Transactions on Neural Systems and Rehabilitation Engineering : A Publication of the IEEE Engineering in Medicine and Biology Society, 23*(5), 755-764. doi:10.1109/TNSRE.2014.2346927 [doi]

Legro, M. W., Reiber, G., del Aguila, M., Ajax, M. J., Boone, D. A., Larsen, J. A., . . . Sangeorzan, B. (1999). Issues of importance reported by persons with lower limb amputations and prostheses. *Journal of Rehabilitation Research and Development, 36*(3), 155-163.

Lehmann, J. F., Price, R., Boswell-Bessette, S., Dralle, A., Questad, K., & deLateur, B. J. (1993). Comprehensive analysis of energy storing prosthetic feet: Flex foot and seattle foot versus standard SACH foot. *Archives of Physical Medicine and Rehabilitation, 74*(11), 1225-1231.

Malzahn, J., Kashiri, N., Roozing, W., Tsagarakis, N., & Caldwell, D. (2017). (2017). What is the torque bandwidth of this actuator? Paper presented at the 4762-4768. doi:10.1109/IROS.2017.8206351

Miller, W. C., Speechley, M., & Deathe, B. (2001). The prevalence and risk factors of falling and fear of falling among lower extremity amputees. *Archives of Physical Medicine and Rehabilitation, 82*(8), 1031-1037. doi:S0003-9993(01)27659-X [pii]

Ott, C., Albu-Schaffer, A., Kugi, A., Stamigioli, S., & Hirzinger, G. (2004). (2004). A passivity based cartesian impedance controller for flexible joint robots - part I: Torque feedback and gravity compensation. Paper presented at the , *3* 2659-2665 Vol.3. doi:10.1109/ROBOT.2004.1307462

Ott, C., Eiberger, O., Friedl, W., Bauml, B., Hillenbrand, U., Borst, C., . . . Hirzinger, G. (2006). (2006). A humanoid two-arm system for dexterous manipulation. Paper presented at the 276-283. doi:10.1109/ICHR.2006.321397

Rouse, E. J., Hargrove, L. J., Perreault, E. J., & Kuiken, T. A. (2014). Estimation of human ankle impedance during the stance phase of walking. *IEEE Transactions on Neural Systems and*

*Rehabilitation Engineering : A Publication of the IEEE Engineering in Medicine and Biology Society*, *22*(4), 870-878. doi:10.1109/TNSRE.2014.2307256 [doi]

Satkunskiene, D., Grigas, V., Eidukynas, V., & Domeika, A. (2009). 487. acceleration based evaluation of the human walking and running parameters. *Journal of Vibroengineering*, *11*(3)

Shepherd, M. K., & Rouse, E. J. (2017). The VSPA foot: A quasi-passive ankle-foot prosthesis with continuously variable stiffness. *IEEE Transactions on Neural Systems and Rehabilitation Engineering : A Publication of the IEEE Engineering in Medicine and Biology Society*, *25*(12), 2375-2386. doi:10.1109/TNSRE.2017.2750113 [doi]

Shultz, A. H., Lawson, B. E., & Goldfarb, M. (2016). Variable cadence walking and ground adaptive standing with a powered ankle prosthesis. *IEEE Transactions on Neural Systems and Rehabilitation Engineering*, *24*(4), 495-505. doi:10.1109/TNSRE.2015.2428196

Sup, F., Varol, H. A., Mitchell, J., Withrow, T., & Goldfarb, M. (2008). Design and control of an active electrical knee and ankle prosthesis. *Proceedings of the ...IEEE/RAS-EMBS International Conference on Biomedical Robotics and Biomechatronics.IEEE/RAS-EMBS International Conference on Biomedical Robotics and Biomechatronics, 2008*, 523-528. doi:10.1109/BIOROB.2008.4762811 [doi]

Torburn, L., Perry, J., Ayyappa, E., & Shanfield, S. L. (1990). Below-knee amputee gait with dynamic elastic response prosthetic feet: A pilot study. *Journal of Rehabilitation Research and Development*, *27*(4), 369-384. doi:10.1682/jrrd.1990.10.0369

Voloshina, A. S., & Collins, S. H. (2019). *A review of design and control approaches in lower-limb prosthetic devices*

Waters, R. L., & Mulroy, S. (1999). The energy expenditure of normal and pathologic gait. *Gait & Posture, 9*(3), 207-231. doi:S0966636299000090 [pii]

Wen, Y., Si, J., Brandt, A., Gao, X., & Huang, H. H. (2020). Online reinforcement learning control for the personalization of a robotic knee prosthesis. *IEEE Transactions on Cybernetics, 50*(6), 2346-2356. doi:10.1109/TCYB.2019.2890974

Zidarov, D., Swaine, B., & Gauthier-Gagnon, C. (2009). Quality of life of persons with lower-limb amputation during rehabilitation and at 3-month follow-up. *Archives of Physical Medicine and Rehabilitation, 90*(4), 634-645. doi:10.1016/j.apmr.2008.11.003 [doi]

Ziegler-Graham, K., MacKenzie, E. J., Ephraim, P. L., Travison, T. G., & Brookmeyer, R. (2008). Estimating the prevalence of limb loss in the united states: 2005 to 2050. *Archives of Physical Medicine and Rehabilitation, 89*(3), 422-429. doi:10.1016/j.apmr.2007.11.005 [doi]

# APPENDICES

# APPENDIX A

## Human Ankle Biomechanics

Before the discussion of design specifications and methods for ankle prosthetic design, it is essential to define and discuss terms about the human gait cycle. For the initial discussion, we consider level-ground human walking, which is defined from the beginning of the heel strike of one foot to the heel strike of the other foot. Regarding the sign convention for ankle movement, the motion of the ankle (or torque) towards the sheen (dorsiflexion) is considered as positive, while movement away from the sheen (plantarflexion) is considered negative (Figure A.1).


**Figure A.1** Directional nomenclature of ankle angle: positive (dorsiflexion on the left) and negative (plantarflexion on the right) motion

The gait cycle is divided into two principal phases: the stance phase and the swing phase. The stance phase represents the foot in contact with the ground (from heel strike to toe-off for the same foot) and accounts for 60% of the entire gait cycle time. The swing phase is characterized by the foot being off the ground and accounts for the remaining 40% of the gait cycle time (Au, *et al.*, 2008). The stance phase can be further subdivided into three sub-phases: Controlled Plantarflexion (CP), Controlled Dorsiflexion (CD), and Powered Plantarflexion (PP), as shown in Figure A.2 below.

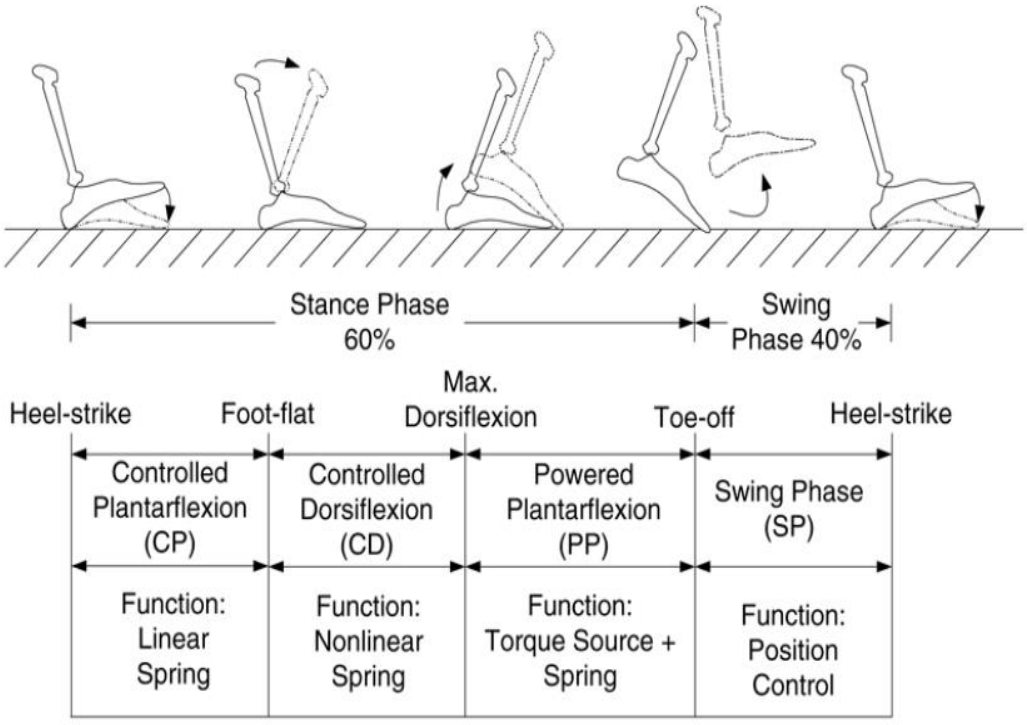


**Figure A.2** The level-ground gait cycle (Au, *et al.*, 2008)

**Controlled Plantarflexion (CP)**

CP starts from the heel strike from the foot and ends when the foot is flat on the ground. The torque exerted by the ground on the foot is plantarflexion since the Center of Pressure (COP) lies behind the ankle as shown in Figure A.3. Hence, the ankle muscles must exert a dorsiflexion torque to lower the foot (plantarflexion). This ankle torque in CP can be characterized as a linear torsional spring with respect to ankle position, with stiffness varying from step to step (constant for a single step).

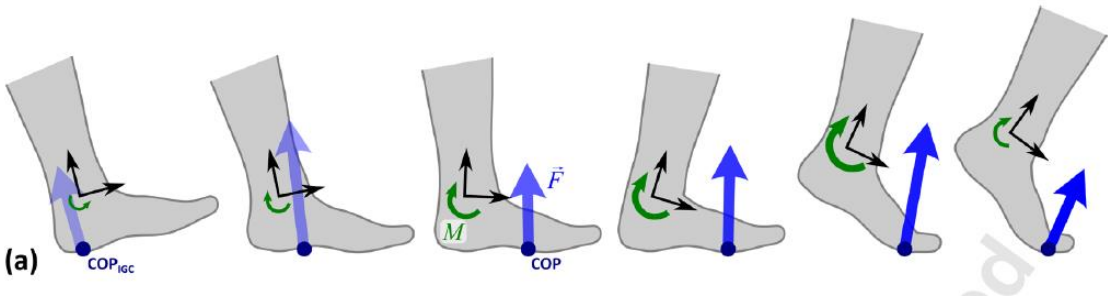


**Figure A.3** Change in the Center of Pressure (COP), ground reaction force F, and moment exerted by the ankle M during level-ground walking (Adamczyk, 2020)

**Controlled Dorsiflexion (CD)**

CD starts from foot flat and extends to a maximum dorsiflexed state, and as with CP, this motion is controlled. The purpose of CD is to store elastic energy and release it during the powered plantarflexion phase to achieve the necessary foot push-off. The ankle torque in CD can be characterized as a nonlinear torsional spring.

**Powered Plantarflexion (PP)**

PP starts at the end of CD and continues until toe-off. The ankle injects energy in this phase, more than compensating for the negative energy stored in CD; for this, PP can be modeled as a power source in parallel with a nonlinear spring. This phase is important for the propulsion necessary for optimal gait.

**Swing (SW)**

SW starts as described before from the toe-off to the heel strike of the same foot. This phase can be characterized as ankle angle motion control and thus the ankle acts as a positive source of energy during this phase.

**Ankle torque-angle characteristics**

An important consideration for the design of ankle prosthetic devices is the Ankle torque vs Ankle Angle curve shown below in Figure A.4. As discussed previously, the CD phase involves storing the energy gained from shifting the weight of the human's body forward and releasing the energy in the form of ankle torque during PP as an assistive function to the motorized actuator. This is the function of the ankle muscles that is mimicked by a passive spring in many prosthetic devices, particularly passive (not externally powered) devices.

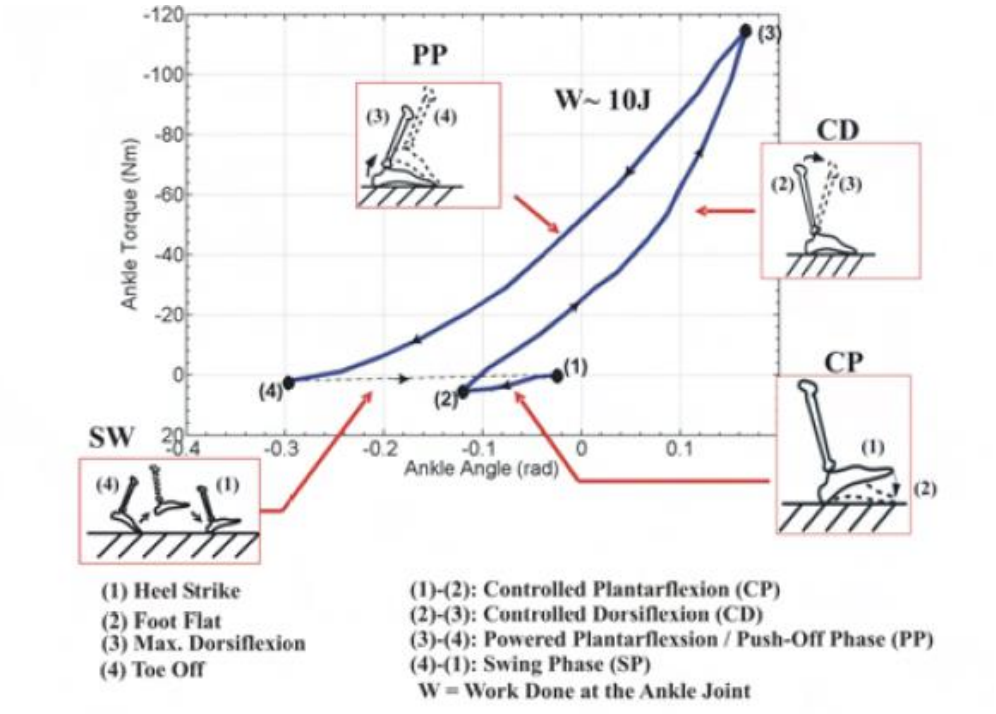


**Figure A.4** Able-bodied Ankle Torque-Angle for a 75 kg individual (Gates, 2004)

# APPENDIX B

## Design flow chart

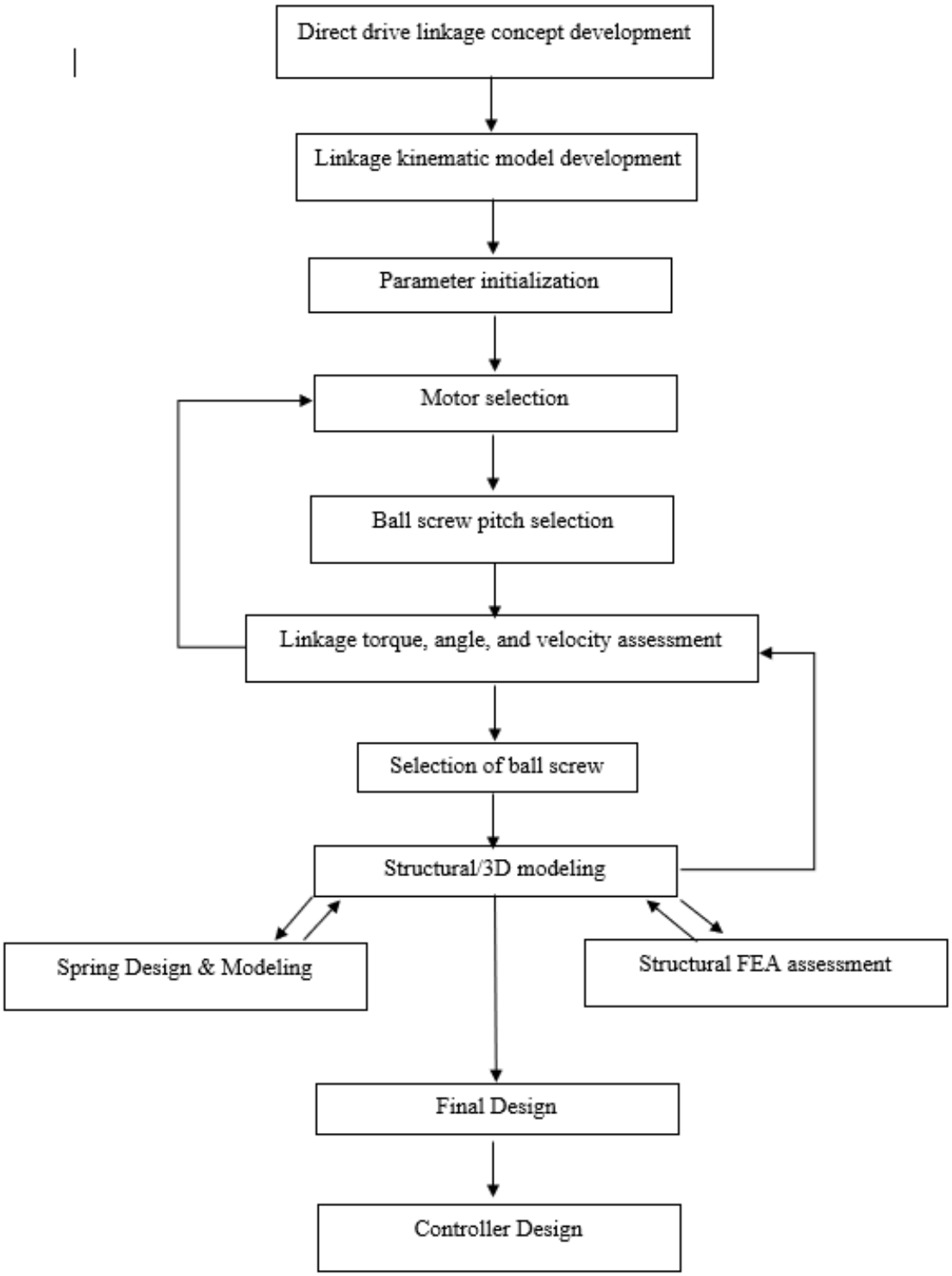

# APPENDIX C

## Comparison of raw, filtered, and desired torque output in the impedance tests shown in Section 3.3.4

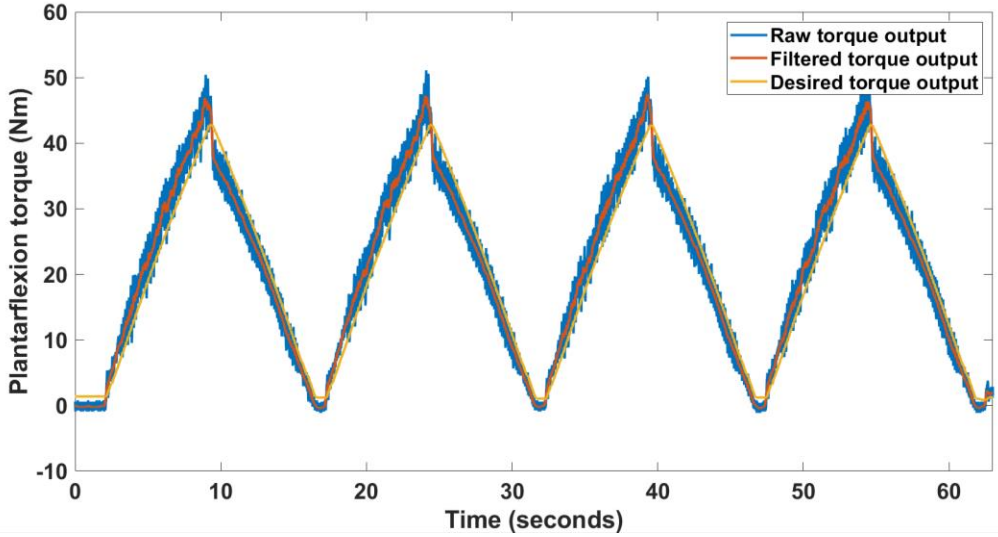


**Figure C.1** Impedance control curves for $k_{PP}$ = 162.4 Nm/rad with a feedback gain $k_f$ = 0.67 (torque-time curve)

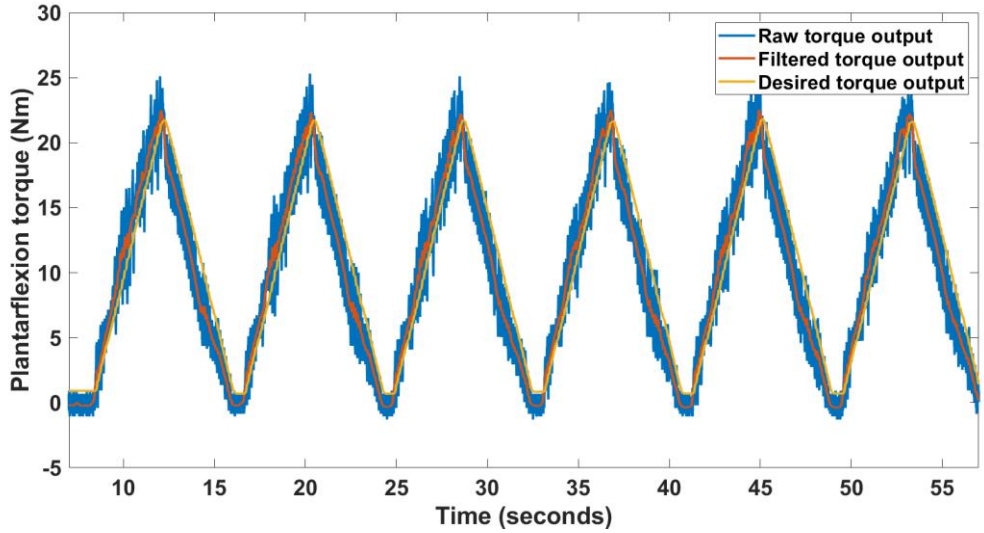


**Figure C.2** Impedance control curves for $k_{CD}$ = 179.2 Nm/rad with a feedback gain $k_f$ = 0.67 (torque-time curve)

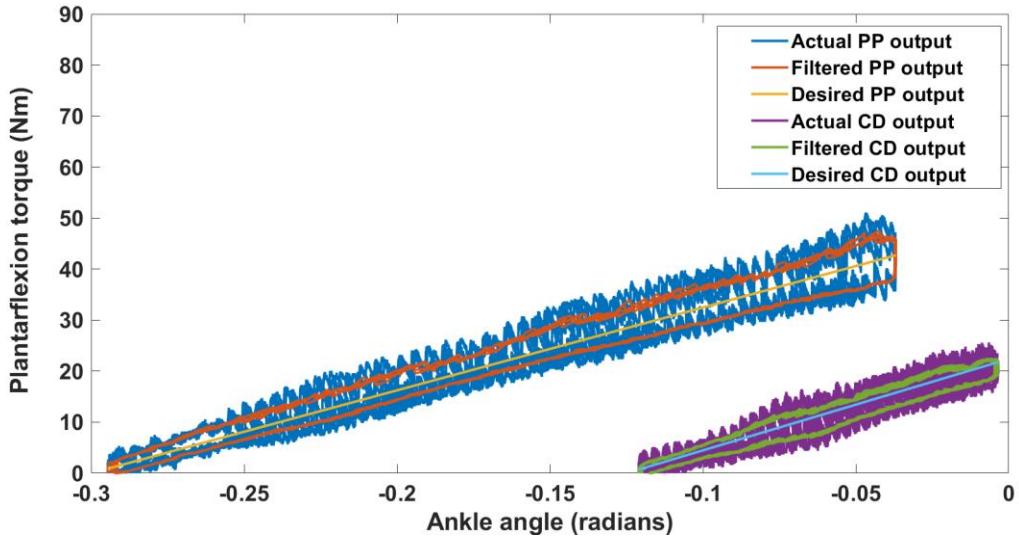


**Figure C.2** Impedance control tests for $k_{PP}$ = 162.4 Nm/rad and $k_{CD}$ = 179.2 Nm/rad for a feedback gain $k_f$ = 0.67 (torque-angle curve)